

# Resolving the Tachocline using Inversion of Rotational Splitting Derived from Fitting Very Long and Long Time Series

SYLVAIN G. KORZENNIK<sup>1</sup> AND ANTONIO EFF-DARWICH<sup>2,3</sup>

<sup>1</sup>Center for Astrophysics | Harvard & Smithsonian, Cambridge, MA 02138, USA

<sup>2</sup>Universidad de La Laguna, Tenerife, 38204, Spain

<sup>3</sup>Instituto de Astrofísica de Canarias, Tenerife, 38206, Spain

## ABSTRACT

We use rotation splittings derived from very long and long time series, namely 25.2, 12.6 and 6.3 year long, computed by Korzennik (2023) independent methodology to characterize the solar tachocline and its variation with latitude and time. We use two different inversion methodologies and a model of the tachocline to derive its position, width and the amplitude of the radial shear. To validate our methodology we present results from simulated rotational splittings, whether including or not random noise commensurable with the current observational precision. We also describe how we leverage the fact that one of our methodologies uses an initial guess that can be chosen to include *a priori* information. In order to try to resolve the tachocline, we increased the radial density of the inversion grid and showed how it affect the inferences. We also show how the trade off between smoothing and noise magnification affects these, as well as the effectiveness of using an informed initial guess. Results derived from high-precision rotational splittings show clearly that the location of the tachocline at low latitudes is different for its position at high latitudes. The latitudinal variation of its width is not significantly constrained, but our results agree with estimates based on forward modeling. When using splittings derived from somewhat shorter time series, we find temporal variations that are neither definitive nor significant, since we see systematic differences when using different methodologies.

*Keywords:* Solar rotation, Tachocline, Inverse Modeling, Helioseismology

## 1. INTRODUCTION

The solar tachocline, a term introduced by Spiegel and Zahn (1992), is the shear layer where the solar rotation transitions from a nearly rigid-body rotation in the radiative interior to a differential rotation in the convection zone, i.e., where the rotation varies with depth and latitude. This transition layer is located near the base of the convective envelope, i.e., approximately at  $0.7 R_\odot$ , and is believed to be the seat of the solar dynamo, the mechanism responsible for generating the Sun’s magnetic field. It is also believed to be responsible for the solar activity cycles and to play a vital role in angular momentum transport and chemical mixing within the Sun (Strugarek et al. 2023).

Over the past three decades, helioseismic analyses of the internal solar rotation rate (Thompson et al. 2003), based on p-mode oscillation frequencies and employing both global and local inversion techniques, have provided increasingly precise estimates of the tachocline’s location, thickness, and temporal variability (see Table 1). These studies rely on observations from instruments such as BBSO (Libbrecht 1989), SDO-HMI (Schou et al. 2012), SOI-MDI (Scherrer et al. 1995), GONG (Harvey et al. 1996), and LOWL (Tomeczyk et al. 1995), which have provided frequency measurements of acoustic modes whose internal turning points are distributed both above and below the tachocline, thereby enabling sensitive diagnostics of this rotational shear layer. Helioseismic results place the tachocline between  $0.69$  and  $0.72 R_\odot$ , with estimates of its thickness at the equator ranging from  $0.006$  to  $0.05 R_\odot$  (see Table 2). Despite general agreement on its location, substantial variation persists across studies, particularly regarding the tachocline’s latitudinal profile and temporal evolution. Some studies suggest a prolate geometry, i.e., thicker and deeper at higher latitudes, while

others suggest a more spherical or indeterminate structure. Similarly, while several analyses detect temporal changes in the amplitude of the shear with respect to time, hence the solar activity level, others find no significant variation.

These discrepancies arise not only from the limited spatial resolution of helioseismic inversions, particularly near the tachocline, but also from differences in the length and quality of the input data sets, the inversion methodologies, and the parameterizations used to define the tachocline properties. In any case, it is clear that the tachocline is a dynamic, spatially complex region whose precise characterization remains challenging. Hence, it is necessary to implement inversion techniques capable of resolving sharp gradients and fine-scale features while minimizing smoothing, typically used to alleviate the intrinsic singular nature of the rotation inverse problem, while limiting noise magnification. Moreover, applying such techniques consistently across diverse data sets derived from different instruments is essential for building a coherent and physically meaningful picture of the tachocline.

Although the present work focuses primarily on the internal rotation rate of the Sun, complementary and essential insights are provided by helioseismic inferences of the Sun's internal structure, particularly those deriving the difference in sound speed between observations and the standard solar model in the vicinity of the tachocline. Structural inversions of helioseismic data reveal a distinct bump in the sound speed profile near  $0.65 R_{\odot}$ , coinciding with the location of the tachocline, where observed values exceed predictions from the standard solar model. This anomaly is generally attributed to compositional differences in the tachocline, particularly the helium mixing that reduces the local mean molecular weight and thereby increases the sound speed (Gough and McIntyre 1998). These structural signatures provide independent constraints on the depth, composition, and mixing processes within the tachocline, and therefore offer valuable complementary results to those derived from rotation inversions (Elliott and Gough 1999; Takata and Shibahashi 2003).

A number of theoretical models have been developed to explain the formation, stability, and confinement of the tachocline — i.e., its remarkable thinness — each emphasizing different physical mechanisms (see a sample of them in Table 3). Hydrodynamic models (e.g., Spiegel and Zahn 1992) propose viscous shear spreading, constrained by anisotropic turbulence, as such mechanism, whereas magnetic confinement models rely on either fossil fields resisting differential shear (Gough and McIntyre 1998) or dynamo-generated oscillatory fields (Forgács-Dajka and Petrovay 2001). Additional models highlight the role of thermal wind balance, meridional circulation, and baroclinic forcing in shaping the tachocline's structure (Rempel 2005; Balbus and Weiss 2010). Predictions for the tachocline's location typically place it near the base of the convection zone (around  $0.69 R_{\odot}$ ), with model-dependent thicknesses ranging from very thin ( $\sim 0.02 R_{\odot}$ ) to more extended ( $\sim 0.1 R_{\odot}$ ). Several models account for latitudinal variation, often predicting a prolate shape (thicker at higher latitudes), and some suggest temporal modulations tied to the solar magnetic cycle or internal dynamo dynamics. While steady-state structures are assumed in some cases, others predict cyclic or irregular variability, reflecting the dynamic interplay between rotational shear, magnetic fields, and turbulent mixing.

Hence, it is essential to improve the observational constraints provided by helioseismic inversions, including isorotation contours, detailed latitudinal and radial shear gradients, confirming the nearly uniform rotation of the radiative interior, and measuring the tachocline's position and thickness as well as their latitudinal variation. These characteristics are essential for understanding its long-term stability against radiative spreading. They are also vital for constraining the underlying angular momentum transport mechanism, like the nature of turbulent anisotropy (e.g., horizontal vs. radial efficiency) and the effectiveness of magnetic confinement by either fossil or dynamo-generated oscillatory fields. Finally, long-term, continuous helioseismic observations with high spatial resolution are required to detect subtle temporal variations of the tachocline potentially linked to the solar cycle or internal dynamo dynamics.

In summary, we need to move beyond broad qualitative descriptions and toward a quantitatively constrained characterization of the tachocline's structure and its role in solar dynamics. This requires not only enhanced spatial resolution, sensitivity, and temporal coverage, but also the systematic application of consistent and robust inversion techniques across multiple data sets and instruments.

## 2. DATA SETS

In order to best characterize the solar tachocline using rotation inversions we want to use rotational splittings with the lowest possible uncertainties, hence values estimated using the longest available time series. In contrast to the instruments' respective reduction pipe-lines, observations taken by MDI, HMI and GONG have been fitted by Korzennik (2023) using time series of various lengths. Namely, sets as short as 36 days, but also sets of 72, 144, 288, etc, up to 2,304 days and 4,608 days (i.e.,  $32 \times$  and  $64 \times 72$  days, or 6.3 and 12.6 years respectively) for all 3

Instrument	Location	Width	Observed Variation	Reference
BBSO	$0.692 \pm 0.005$	$0.096 \pm 0.04$		Kosovichev (1996)
Mean GONG+BBSO	$0.7050 \pm 0.0027$	$0.0098 \pm 0.0026$		Basu (1997)
GONG	$0.675 - 0.695$	$0.001 - 0.013$	Hints of latitude dependence, not statistically significant. Dependence on the analysis technique	Antia, Basu & Chitre (1998)
LOWL	$0.695 \pm 0.005$	$0.05 \pm 0.03$	(half-width)	Corbard et al. (1998)
LOWL	$0.701 \pm 0.004$	$< 0.05$		Corbard et al. (1999)
LOWL	$0.693 \pm 0.002$	$0.039 \pm 0.013$	Prolate profile: radius increases by $\sim 0.024 \pm 0.004 R_\odot$ from equator to $60^\circ$ . No significant variation of thickness with latitude	Charbonneau et al. (1999)
MDI	$0.697 \pm 0.002$	$0.019 \pm 0.001$	Based on inversions of the sound speed	Elliott & Gough (1999)
	Not specified	Not specified	Rotation rate increases with depth at low/mid latitudes, 1.3-year oscillations near equator, $\sim 1$ year at high latitudes	Howe et al. (2000)
Mean GONG+MDI	$0.6893 \pm 0.0023$	$0.0061 \pm 0.0012$	Clear latitudinal variation in depth. No significant temporal variations	Basu & Antia (2001)
Mean GONG+MDI	$0.6916 \pm 0.0019$	$0.0065 \pm 0.0013$	Clear latitudinal variation in depth and width. No significant temporal variations	Basu & Antia (2003)
GONG	$0.6945 \pm 0.0013$	$0.0037 \pm 0.0011$	Center is prolate and thickness increases with latitude	Antia & Basu (2011)
MDI	$0.6915 \pm 0.0016$	$0.0028 \pm 0.0017$	Clear temporal variation of $\delta\Omega$ with solar activity	
GONG	$0.7067 - 0.7187$	$0.0067 - 0.0198$		
MDI	$0.708 - 0.7181$	$0.003 - 0.0188$	Clear temporal variation across solar cycles 23–25, changes in depth and $\delta\Omega$	Basu et al. (2024)

**Table 1.** Summary of tachocline properties from various helioseismic studies. Observed variations include only latitudinal or temporal effects when reported.

Instrument	Position	Width
MDI	0.692 – 0.718	0.003 – 0.072
GONG	0.689 – 0.719	0.006 – 0.096
LOWL	0.690 – 0.700	0.026 – 0.080
BBSO	0.690 – 0.696	0.031 – 0.080
HMI	0.706 – 0.717	0.008 – 0.018

**Table 2.** Summary of the position and width of the tachocline at the equator as estimated from each instrument.

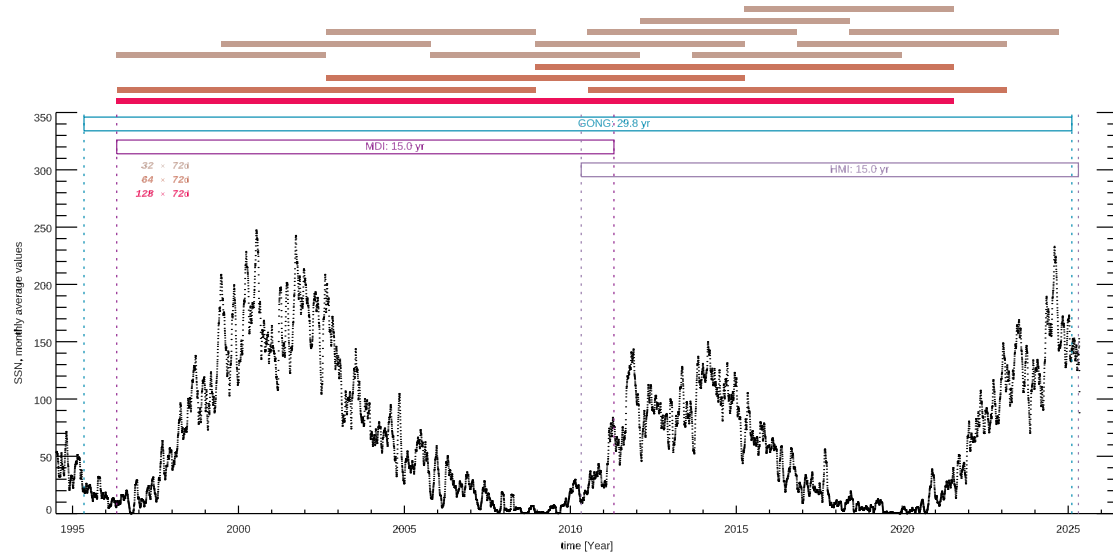


**Figure 1.** Temporal coverage of the time series used in the work presented here (filled boxes), compared the temporal coverage of the observations (open boxes) for the MDI, HMI and GONG instruments, and to the solar activity illustrated by the monthly averaged sunspot number.

instruments, and up to 9,216 days (i.e.,  $128 \times 72$  days, or 25.2 years) for GONG. For time series longer than 72 days, the fitted epochs overlap by 50%, while their starting time is offset by an integer multiple of 72 days with respect to 1996.05.01 (i.e., the first day MDI produced science quality data).

To attempt resolving the tachocline, we opted to use rotational splittings resulting from fitting a very long (i.e.,  $128 \times 72$  day) and long (i.e.,  $32 \times$  and  $64 \times 72$  day) time series. The temporal coverage of these time series, compared with that of the three instruments, as well as the solar activity, represented by the sunspot number, are plotted in Fig. 1.

### 3. METHODOLOGY AND INVERSE TECHNIQUES

#### 3.1. Variable Radial Gridding

Since we try to resolve the tachocline, we decided to break from tradition and use a model grid – i.e., the set of target locations – with a high resolution in the radial direction, especially around the tachocline. The resolution in latitude was in all cases left uniform. Since our inversion techniques (see below) allow for a variable grid spacing, we experiment with various grids. Of course, the simplest grid is a uniformly spaced grid, but in order to reach a high resolution at the tachocline (i.e., well below 0.5% in the radial direction) the grid size becomes large, hence the size of the problem (i.e., the sizes of the matrices to handle) gets very large, requiring large amounts of memory and quite long computation time. With these constraints in mind, we defined such a grid using 256 radial points and 54 latitudinal points, or 13,824 target locations. The radial resolution of this grid is 0.39%.

**Table 3.** Summary of some theoretical tachocline confinement models and their predictions.

Confinement Mechanism	Properties, if given	Reference
Confinement due to highly anisotropic turbulent viscosity with a large horizontal component	Width $\sim 0.13$ to $0.1 R_\odot$	Spiegel and Zahn (1992) Elliott (1997)
Magnetic field quenches shear in RZ	Thin implied; thickness increases towards the poles	Rudiger and Kitchatinov (1997)
Fossil magnetic field suppresses shear in RZ explains rigid interior rotation	Thin (i.e., below helioseismic inversion spatial resolution)	Gough and McIntyre (1998) Garaud and Garaud (2008)
Turbulent tachocline pervaded and confined by a dynamo-generated field	Thin	
Anisotropy in momentum transport due to large horizontal turbulent viscosity	Implied thinness	Forgács-Dajka and Petrovay (2001)
Global dynamical model, but is not able to avoid tachocline spreading with time	Base convection zone	Leprovost and Kim (2006)
Baroclinic radiative equilibrium with no significant meridional circulation for stable confined tachocline	Thin and sharp layer	Brun et al. (2011)
This model does not explain tachocline confinement	Much thicker above $50^\circ$ to avoid hydrodynamic instability	Caleo et al. (2015)
Persistent nonaxisymmetric dynamo field regulates tachocline shear via Maxwell stresses	Width $< 0.05 R_\odot$	Gilman (2018)
		Matilsky <i>et al.</i> (2024)

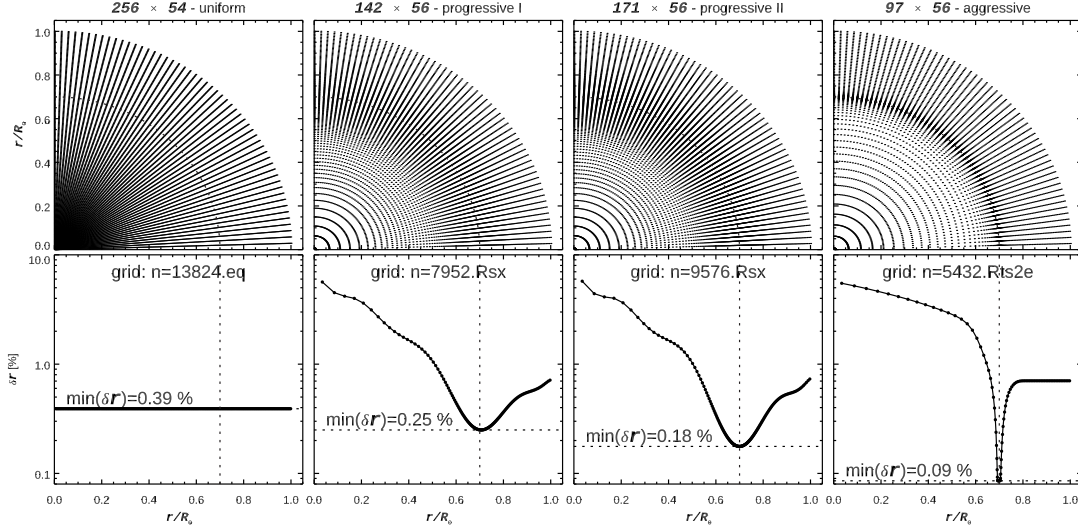


**Figure 2.** Positions of the target locations, shown in Cartesian coordinates (top panels) and the grids' radial spacing as a function of radius (bottom panels) for the four grids we used. Shown, from left to right, are the uniform radial spacing grid, two *progressive* radial spacing grids and the so-called *aggressive* radial spacing grid. The lowest radial resolution, occurring around the tachocline, is indicated as well.

Alternatively, one can change the grid spacing to be large in the radiative zone (i.e., below the tachocline), where one knows from past experience that the radial resolution of rotation inversions is low while the solar rotation rate does not appear to vary much with respect to radius. One can also set the spacing above the tachocline (i.e., in the convection zone) to a value small enough to resolve the known radial variation on that region, while using, in a radial range centered around the tachocline, a much smaller spacing. To avoid edge effects, we realized through trial and error, that it is best if the second derivative of the radial grid remains smooth. Following these guidelines, we defined what we call an *aggressive* grid, a grid that reaches at the tachocline a resolution of 0.09% while remaining a set of 97 by 56, or only 5,432 target locations.

Finally, we also defined what we call *progressive* grids, where the radial spacing was set to vary more smoothly, i.e., using a polynomial in  $r$ , with two target resolutions at the tachocline of 0.25% and 0.18%, hence a set of 142 by 56 or 7,952 target points and a set of 171 by 56 or 9,576 target points.

These 4 grids are illustrated in Fig. 2 where the positions of the target locations are shown in Cartesian coordinates, as well as the corresponding grid radial spacing as a function of radius.

### 3.2. Inversion Techniques

We use two different inversion methods: a variant of the classical regularized least squares technique (RLS, see [Eff-Darwich and Pérez Hernández 1997](#)) and a newly developed iterative technique based on the simultaneous algebraic reconstruction technique (SART, [Korzeniak and Eff-Darwich 2024](#)). The SART technique was originally implemented to solve linear systems in image reconstruction ([Anderson and Kak 1984](#); [van der Sluis and van der Vorst 1990](#)) and was proposed as an inversion technique for the solar internal rotation rate by [Eff-Darwich \*et al.\* \(2010\)](#).

Both methods use a piecewise constant discretization of the two-dimensional rotation inverse problem, and their implementation allows for a non-uniform discretization grid (aka target locations). Both are coded to allow the computation of the averaging kernels,  $K_{i,j}^{(a)}(r, \theta)$ . Indeed, the two-dimensional rotation inverse problem can be written as

$$\frac{\delta\nu_{n,\ell,m}}{2m} = \iint K_{n,\ell,m}^{(r)}(r, \theta) \Omega(r, \theta) dr d\theta \quad (1)$$

where  $\delta\nu_{n,\ell,m} = \nu_{n,\ell,m} - \nu_{n,\ell,-m}$  are the individual rotation splittings,  $\nu_{n,\ell,m}$  the frequency for the mode with radial order  $n$ , spherical harmonic degree  $\ell$ , and azimuthal order  $m$ .  $K_{n,\ell,m}^{(r)}$  is the corresponding rotation kernel (see [Hansen](#),

Cox and van Horn 1977; Eff-Darwich and Pérez Hernández 1997; Korzennik and Eff-Darwich 2024),  $\Omega$  the rotation rate,  $r$  the radius, and  $\theta$  the co-latitude.

Notice that we use the individual rotation splittings, not expansion coefficients of these splittings as a function of  $m$ , since (i) the tables resulting from the fitting by Korzennik (2023) provide these individual frequencies from which we compute the splittings; and (ii) using individual splittings results in better angular resolution since the observables are not pre-smoothed to an arbitrary number of expansion coefficients.

When that inverse problem is solved as a linear combination of the splittings, the resulting estimate of the rotation rate,  $\tilde{\Omega}$ , is a convolution of the *true* underlying rotation rate,  $\Omega$ , by a linear combination of the rotational kernels. That linear combination is the averaging kernel, namely:

$$\tilde{\Omega}(r_i, \theta_j) = \sum_{n,\ell,m} c_{n,\ell,m}^{(i,j)} \frac{\delta\nu_{n,\ell,m}}{2m} \quad (2)$$

$$= \iint \sum_{n,\ell,m} c_{n,\ell,m}^{(i,j)} K_{n,\ell,m}^{(r)}(r, \theta) \Omega(r, \theta) dr d\theta \quad (3)$$

$$= \iint K_{(i,j)}^{(a)}(r, \theta) \Omega(r, \theta) dr d\theta \quad (4)$$

hence

$$K_{(i,j)}^{(a)}(r, \theta) = \sum_{n,\ell,m} c_{n,\ell,m}^{(i,j)} K_{n,\ell,m}^{(r)}(r, \theta) \quad (5)$$

Our RLS technique is computationally fast, and we implemented it with a single trade-off parameter (aka Lagrangian multiplier) that controls the amount of smoothing on the solution by minimizing its second derivative. In contrast, the SART technique is slow, since it is an iterative method, and we implemented it using either a global or local smoothing. The local smoothing is a parametrized function of depth and latitude (see Korzennik and Eff-Darwich 2024, for additional details). Since there is some commonality in the pre-processing of both methods, i.e., the discretization of matrices on the model grid, that common first step is coded as a separate computation, and is parallelized using the message passing interface (MPI) to speed it up. The second step of the SART inversion is also parallelized using MPI, while the second step of the RLS is not since it is relatively fast.

Finally, since the SART technique starts with an initial guess, it gives us the option to use either a simple starting value, like a constant close to the mean rotation rate, or an informed initial guess, like a two-dimensional approximation of the anticipated solution.

### 3.3. SART Initial Guess

The simplest way to define the SART initial value is to start with a constant value at each grid point, picking a value close to the mean rotation. Hence we selected a starting value of 470 nHz. We also checked that we run enough iterations for the technique to converge, by saving the solution at intermediate number of iterations and confirming that the changes of the solution become negligible.

We also investigated whether we can exploit the need for a starting value by using an informed guess. If we assume that the solution obtained with the RLS technique is a smoothed version of the true rotation, we should be able to use it to produce such informed initial guess. Since we are interested in the properties of the tachocline, and specifically its width, let us assume that the RLS solution is a good initial guess, but should be sharpened, since the RLS regularization is smoothing of the true solution, while the inferred position of the tachocline does not need any adjustment.

Our current implementation of such sharpening is to fit a sigmoid to the tachocline, assume that its location is correct, but that its width is overestimated. Therefore we replace a portion of the RLS solution by a more narrow sigmoid, typically reducing its width by a factor two, and using this narrow profile as an initial guess for the SART technique.

As presented in the next section, we used simulated splittings computed from model rotation profiles to not only test how well our techniques recover the tachocline, but also to validate our SART initial guess approach.

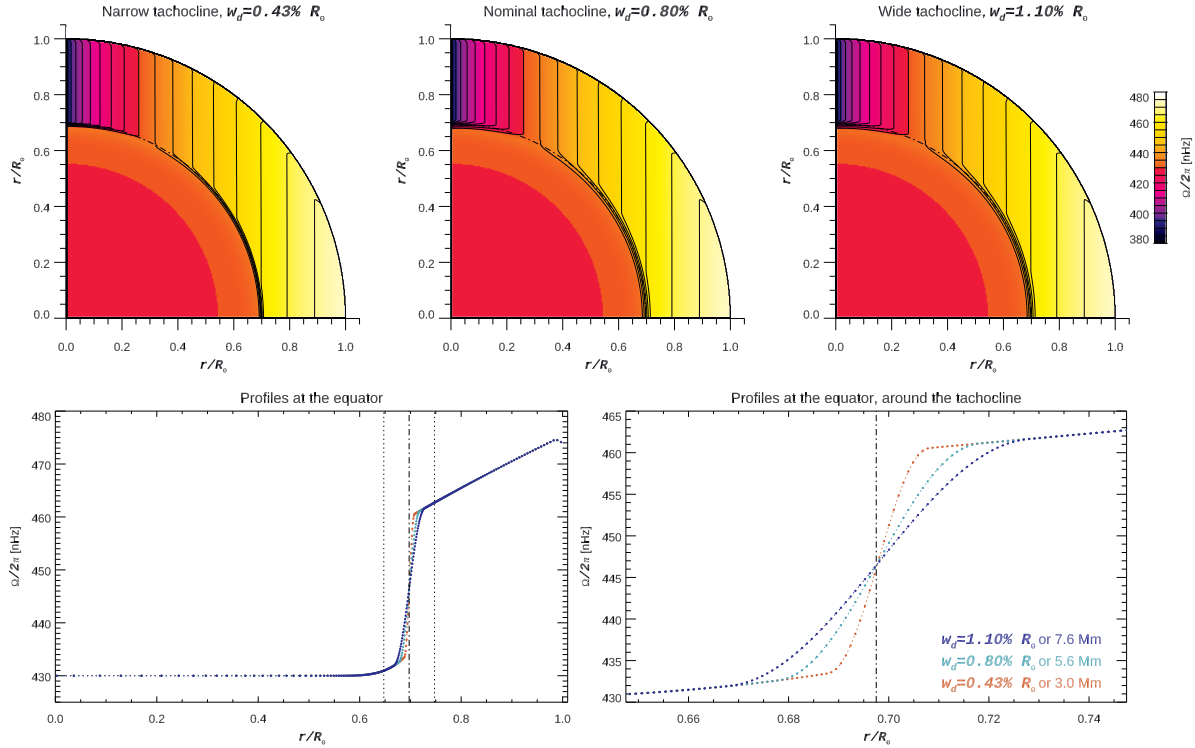


**Figure 3.** Three models used for our simulation. The top panels show the simulated rotation rate in Cartesian coordinates, while the bottom panels show the rotation profile at the equator, with a zoomed view around the tachocline in the lower left panel.

#### 4. RESULTS FROM SIMULATIONS

We present results from simulated splittings computed from simple but realistic rotational models. Namely a solid body rotation below the tachocline, a differential rotation above the tachocline, although constant on cylinder (to use a simple parametrization) and a tachocline whose width is different for different models. From these models, we compute the individual rotational splittings and assign to each an uncertainty corresponding to the error bar for that mode derived from fitting a  $32 \times 72$  day long time series. Assigning a realistic relative uncertainty is key to replicating adequately the resolution potential of observations, even when inverting noiseless splittings. These three models are illustrated in Fig. 3, for a so-called *wide*, *nominal*, and *narrow* tachocline.

Of course, to estimate the effect of observational noise, we also added random noise to each splitting. This noise is scaled by the mode's uncertainty and an arbitrary factor. We used the values 0.1, 0.5 and 1.0 for that extra factor, simulating random errors corresponding to fitting a  $100 \times 4 \times$ , or  $1 \times (32 \times 72\text{-day})$  long time series.

##### 4.1. Noiseless Simulations

The effect of radial gridding on solutions derived from noiseless simulations is shown in Fig. 4 for the RLS method and in Fig. 5 for the SART method, whether using as an initial guess a constant value, or the exact solution.

These figures show clearly how the RLS solution with a very high radial resolution resolves the tachocline, when using a very low smoothing trade-off. It also hints at a Gibbs-like phenomenon in the case of the narrow tachocline.

For the SART method, the solutions computed using the very high radial resolution display numerical noise that we trace to the rate of change of the radial grid. Indeed, this noise is absent from the solutions for the the progressive grids. Not surprisingly, the solutions for noiseless simulations, when starting with the exact solution and when using very little smoothing, recover the narrow tachocline. Yet adding more radial points to reach a lower minimum resolution, using a progressive grid, recovers the solution even better. And, not surprisingly either, adding some smoothing, in all cases, leads to a set of solutions that no longer resolves the model with the most narrow tachocline.

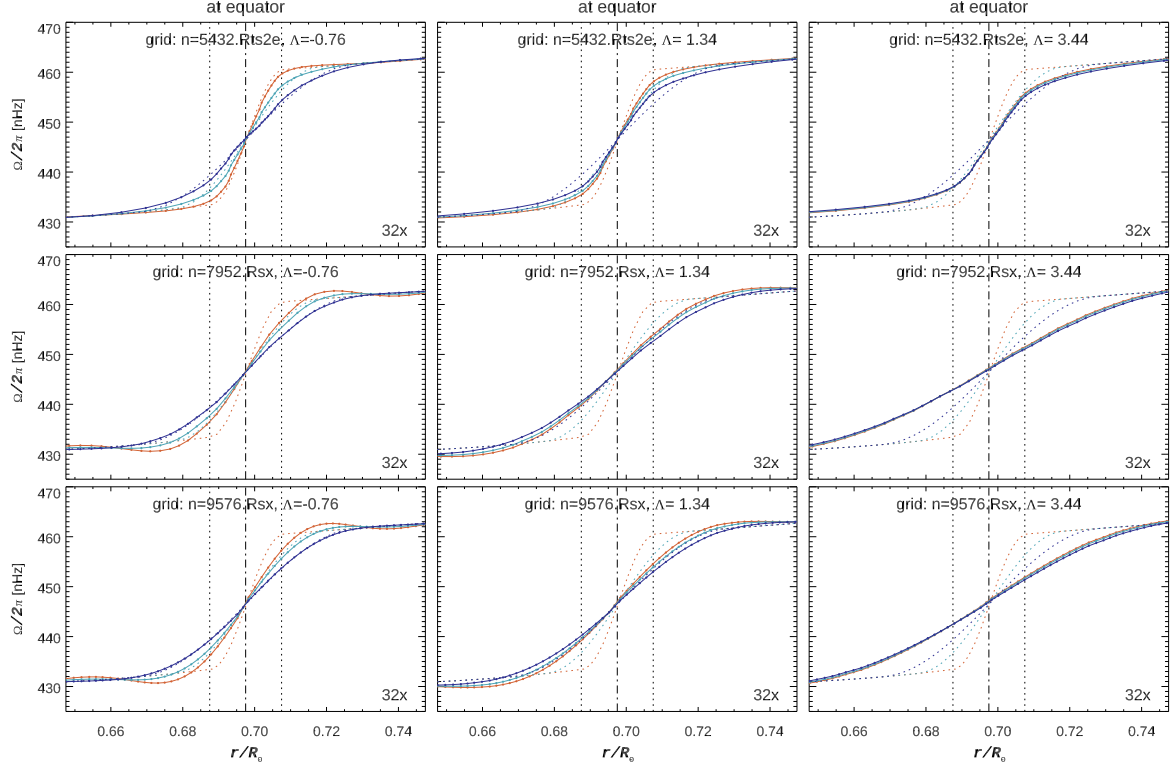


**Figure 4.** RLS solutions for noiseless simulations (solid lines with dots) superimposed over the true solutions (dashed lines) for the three models of the tachocline, shown using different colors (red for *narrow*, green for *nominal*, and blue for *wide*). Top to bottom panels correspond to different inversion grids (*aggressive*, *progressive I*, and *progressive II*), while left to right panels correspond to increasing smoothing (as per the trade-off coefficient  $\Lambda$ ).

We also need to check the effect of the choice of the initial guess, since except for simulations, the exact solution is unknown. Henceforth we inverted noiseless simulated data sets starting with a narrow, nominal or wide initial guess for all 3 simulations (i.e., models with narrow, nominal, and wide tachocline). The resulting solutions when using almost no smoothing are presented in Fig. 6, while solutions when using what we consider typical smoothing are shown in Fig. 7. These plots indicate that in the absence of noise and with almost no smoothing, the SART method with a too narrow initial guess will not properly recover the wider tachoclines, yet this becomes less of a problem when including typical smoothing.

#### 4.2. More Realistic Simulations

Since in practice actual observations have some level of noise, it is a lot more instructive to invert simulations with random noise. Solutions for noisy simulations using the RLS method are presented in Fig. 8 and when using the SART method, and two levels of smoothing, in Fig. 9.

What these figures show is that in the presence of noise, the RLS and SART solutions display a strong Gibbs-like effect. While RLS solutions using the so-called aggressive grid looked great when using noiseless splittings, adding any level of noise results in large excursions that gets damped with additional smoothing.

The challenge when using actual observations remains the optimal and objective selection of the trade-off between smoothing and noise amplification. Yet, with these caveats in mind, using the aggressive radial grid remains a viable strategy. In contrast, the SART method behaves a lot better when using the progressive grid, but remains affected by Gibbs-like excursions without appropriate smoothing. Yet, using an informed initial guess, while tricky and misleading in noiseless cases, offers limited improvement in the noisy cases.

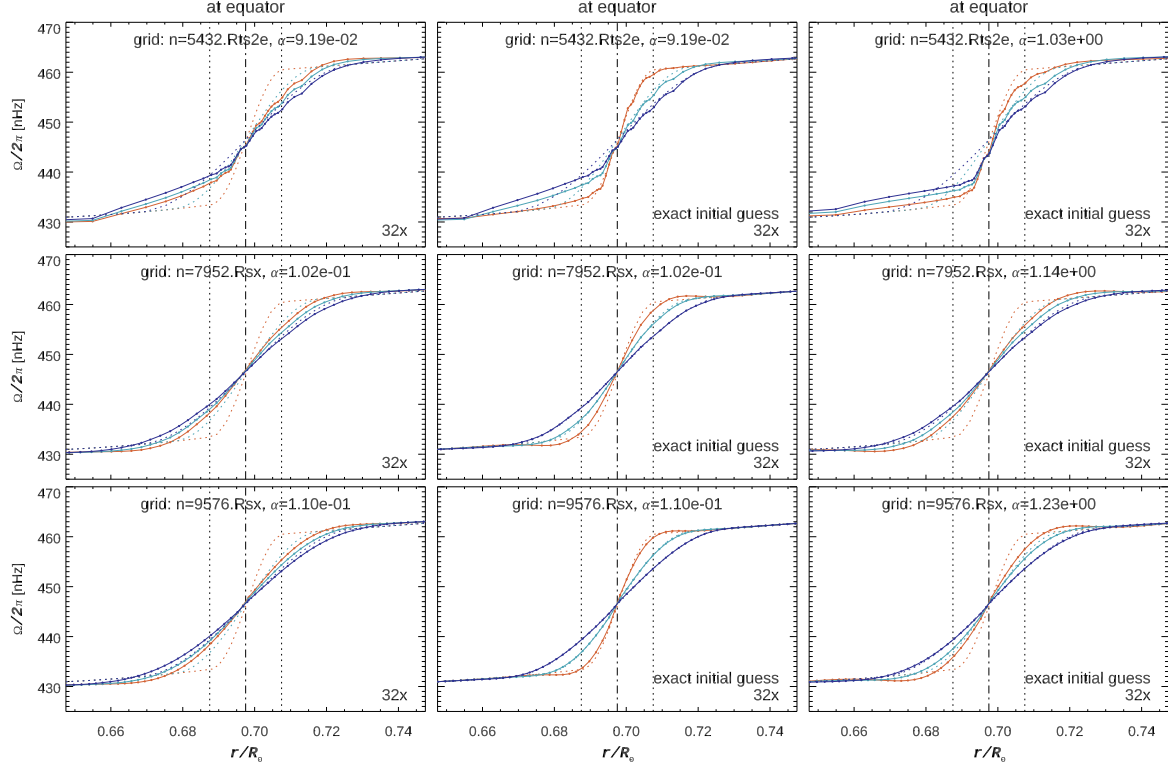


**Figure 5.** SART solutions for noiseless simulations (solid lines with dots) superimposed over the true solutions (dashed lines) for the three models of tachocline, shown using different colors (red for *narrow*, green for *nominal*, and blue for *wide*). Top to bottom panels correspond to different inversion grids (*aggressive*, *progressive I* and *progressive II*), while leftmost panel shows solutions when initial guess is set to a constant, while the middle and rightmost panels correspond to solutions when setting the initial to the true solutions and varying the smoothing factor  $\alpha$  (i.e., smoothing increases with lower  $\alpha$  values). The unique combination of the *progressive II* grid, exact initial solution and low smoothing (in the lowest middle panel) recovers almost perfectly the three models.

## 5. RESULTS FROM OBSERVATIONS

From the tables of individual modes,  $\nu_{n,\ell,m}$ , we compute the scaled rotational splittings,  $s_{n,\ell,m}$ , and perform an outliers rejection. The scaled rotational splittings are defined as

$$s_{n,\ell,m} = \frac{\delta \nu_{n,\ell,m}}{2m} \quad (6)$$

The uncertainties of the scaled splittings,  $\sigma_{s_{n,\ell,m}}$ , are derived from the individual modes uncertainties.

The outliers rejection consists in fitting a straight line to the scaled splittings,  $s_{n,\ell,m}$ , with respect to the ratio  $m/\ell$ , using a  $3\sigma$  rejection when performing this fit. Scaled splittings that depart from that straight line by some value,  $r_s$ , are rejected, i.e., when

$$|s_{n,\ell,m} - f\left(\frac{m}{\ell}\right)| > r_s \quad (7)$$

as well as values whose reduced differences magnitude, i.e., the difference divided by the uncertainty, exceed some threshold,  $t_s$ , i.e., when

$$\left| \frac{s_{n,\ell,m} - f\left(\frac{m}{\ell}\right)}{\sigma_{s_{n,\ell,m}}} \right| > t_s \quad (8)$$

We tested several combinations of these two thresholds and settled on  $r_s = 200$  nHz and  $t_s = 1.5$  as a good trade-off between limiting the amount of rejection and yet eliminating most of the outliers.

The resulting rotational rates, for four data sets and both inversion methods, are shown in an overall two-dimensional representation in Cartesian coordinates in Fig. 10. The main features of the resulting rotation rate are the well-

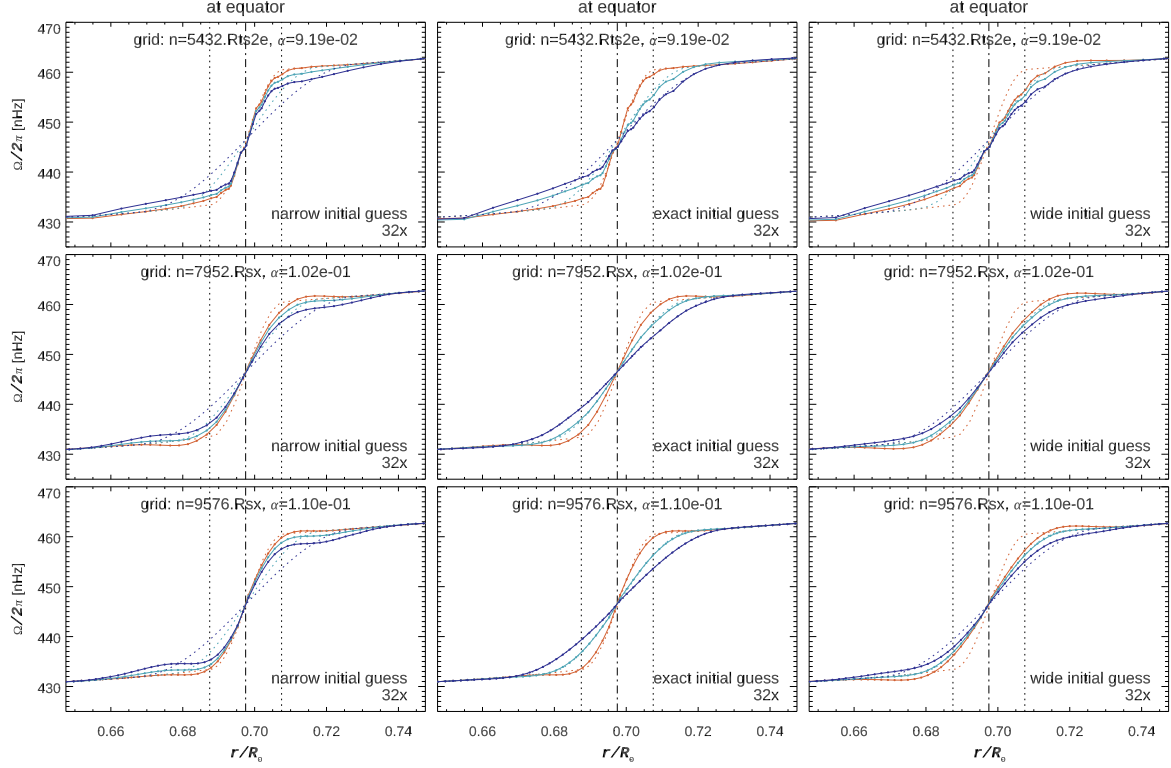


**Figure 6.** SART solutions for noiseless simulations (solid lines with dots) superimposed over the true solutions (dashed lines) for the three models (shown with different colors) and almost no smoothing. Top to bottom panels correspond to different inversion grids (*aggressive*, *progressive I* and *progressive II*), while left to right panels correspond to using different initial guesses (narrow, exact and wide respectively).

established near solid body rotation in the radiative interior, the differential rotation nearly constant on cones in the convection zone, a narrow tachocline near the base of the convection zone and a near-surface shear layer.

### 5.1. Results Using Very Long Time Series

A different representation of the inverted rotation rate derived from fitting a very long time series is shown in Fig. 11, when using in both cases the lower resolution progressive grid. The tachocline and the near-surface shear are clearly visible.

In order to characterize the tachocline, we followed the methodology used in Basu et al. (2024) where the tachocline is parametrized as a sigmoid. Hence, at each latitude, we fit a sigmoid, complemented by two slopes and a constant, to the inverted profiles as a function of radius, namely

$$\tilde{\Omega}(r, \phi) = \Omega_{o,\phi} + \frac{\Delta\Omega_\phi}{1 + e^{\frac{r-r_{d,\phi}}{w_{d,\phi}}}} + \begin{cases} s_{-,\phi} (r - r_{d,\phi}) & \text{for } r < r_{d,\phi} \\ s_{+,\phi} (r - r_{d,\phi}) & \text{for } r > r_{d,\phi} \end{cases} \quad (9)$$

where  $\tilde{\Omega}$  is the inverted rotation rate,  $r$  the radius,  $\phi = \pi/2 - \theta$  the latitude,  $r_{d,\phi}$  the location of the sigmoid discontinuity,  $w_{d,\phi}$  the width of the sigmoid,  $\Delta\Omega_\phi$  the amplitude of the sigmoid jump,  $\Omega_{o,\phi} + \frac{\Delta\Omega_\phi}{2}$  is the rotation at  $r = r_d$  and  $(s_{-,\phi}, s_{+,\phi})$  the slopes below or above  $r_{d,\phi}$ .

We use the limited radial range  $0.43 < r/R_\odot < 0.97$  to fit this model, and note that by including slopes, the actual amplitude of the tachocline jump is given, at each latitude, by

$$\Delta\Omega_{J,\phi} = \Delta\Omega_\Phi \left( \frac{e^{F_\epsilon} - 1}{e^{F_\epsilon} + 1} \right) + (s_{+,\phi} + s_{-,\phi}) F_\epsilon w_{d,\phi} \quad (10)$$

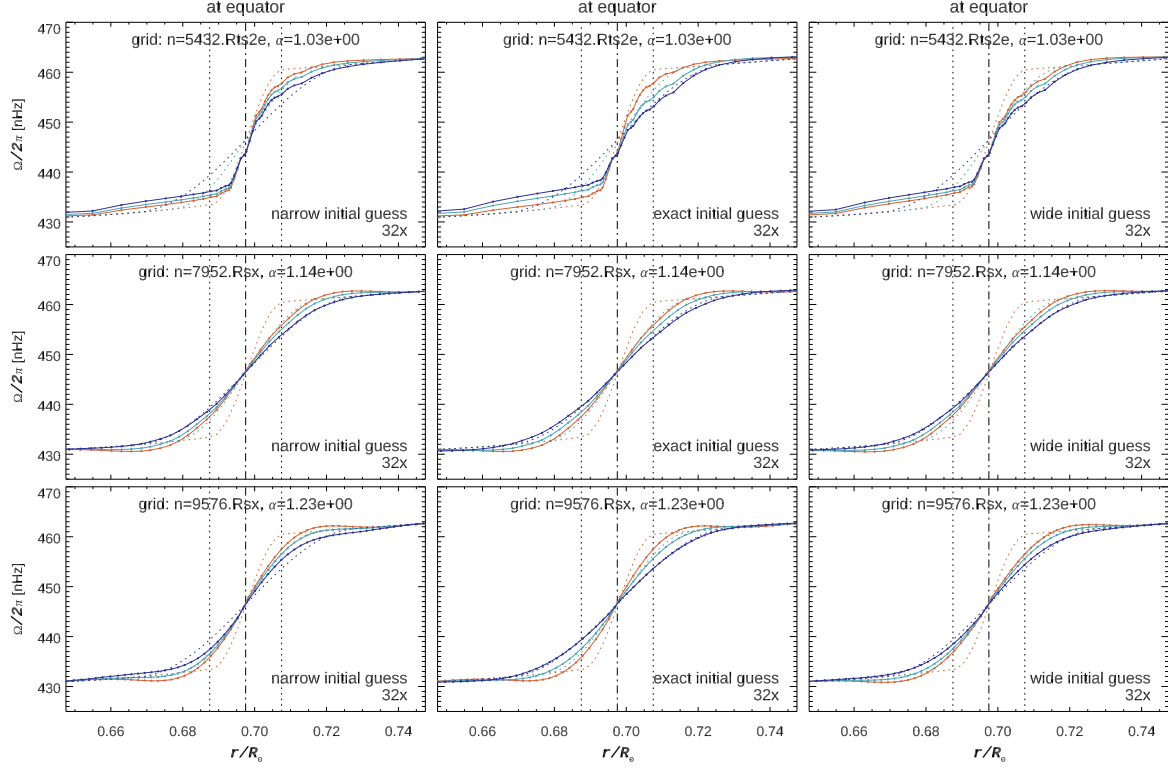


**Figure 7.** SART solutions for noiseless simulations (solid lines with dots) superimposed over the true solutions (dashed lines) for the three models (shown with different colors) and “typical” smoothing. Top to bottom panels correspond to different inversion grids (*aggressive*, *progressive I* and *progressive II*), while left to right panels correspond to using different initial guesses (narrow, exact and wide respectively).

where  $F_\epsilon = \log(\frac{1}{\epsilon} - 1)$ . We chose to evaluate this for  $\epsilon = 0.5 \times 10^{-3}$ , namely the range for which the sigmoid goes from  $\epsilon$  to  $1 - \epsilon$ , or 0.999 of its variation, hence  $F_\epsilon = 7.6$ .

### 5.2. Tachocline Characteristics

The parameters resulting from fitting our sigmoid model to inverted rotations inferred from splittings determined by fitting the 25.2 year long GONG time series are shown in Fig. 12. The total jump,  $\Delta\Omega_J$ , the location,  $r_d$ , and the thickness,  $w_d$ , are plotted as a function of latitude, when using either inversion method, or when using the SART inversion with a narrow initial guess, and for four different inversion grids. Not surprisingly the sigmoid model fitting fails at latitudes where the amplitude of the jump is marginal, since the jump changes sign between low and high latitudes (i.e., around  $\phi = 32^\circ$ ).

These estimates of the total jump around the tachocline,  $\Delta\Omega_J$ , are, up to  $60^\circ$ , consistent whatever method or grid is being used, except for the aggressive grid at high latitudes. The estimates of the location of the tachocline,  $r_d$ , are also overall consistent with respect to the inversion methodology or inversion grid, with some notable exceptions. For all cases, one salient feature is a discontinuity of that location between values derived at low and high latitudes. That discontinuity is more pronounced for the RLS solutions and the precise location at the higher latitudes is somewhat grid dependent. As for estimates of the thickness of the tachocline,  $w_d$ , the figures show some inconsistencies between methodology (i.e., the RLS returning systematically a wider tachocline), but more significantly the estimated width gets smaller as the resolution of the grid around the tachocline gets smaller. Hence, despite its pitfalls, inversions that use the high resolution aggressive grid infer that the tachocline is quite narrow, namely with a FWHJ<sup>4</sup> below 1%.

<sup>4</sup> The full width for half jump, i.e., the radial extent of 50% of the jump, or from 25% to 75%, is  $2.2 w_d$ , or  $2 F_\epsilon w_d$  with  $F_\epsilon$  estimated for  $\epsilon = 0.25$ .

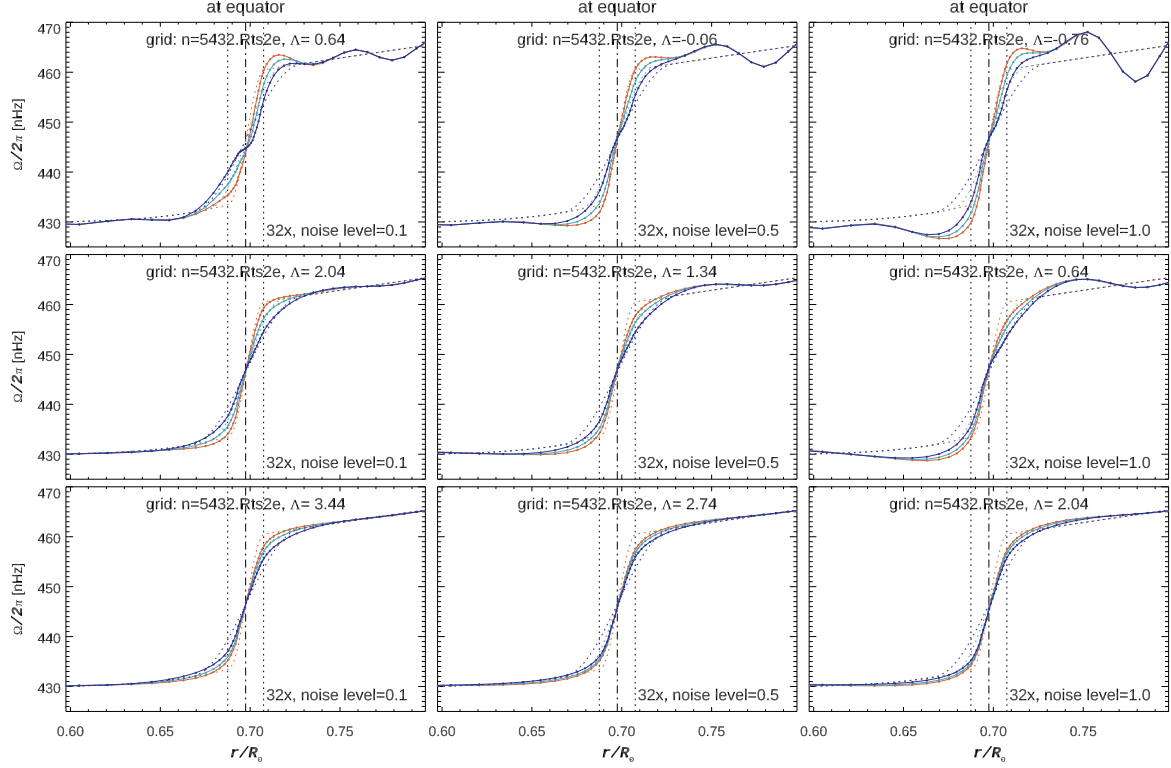


**Figure 8.** RLS solutions for noisy simulations (solid lines with dots) superimposed over the true solutions (dashed lines) for the three models (shown with different colors). Top to bottom panels correspond to increasing smoothing (as per the trade-off coefficient  $\Lambda$ ), while left to right panels correspond to increasing levels of noise, with respect to the uncertainties resulting from fitting a  $32 \times 72$ d time series.

These consistencies and inconsistencies (i.e., inferences from different methods and different grids) are consistent with the results of our simulations.

### 5.3. Effective Location and Averaging Kernels

A possible concern on the robustness of the derived characteristics of the tachocline using the fitting of a sigmoid model, as shown in Fig. 12, is the issue of “*effective location*.” Indeed the estimate of the rotation rate inferred by inversions is the convolution of the underlying *true* solution by the corresponding averaging kernels, not the true value at the target location. Therefore we checked if this convolution is not displacing in a significant way the effective location of the inferred rate from the target location.

In order to assess this we need to define this effective location and decided to use the center of gravity of the averaging kernels. To get an accurate measure of the center of gravity, we computed these averaging kernels on a much higher density grid than the inversion grid, yet not as high as the grid used to compute the rotational kernels, since using such a very high resolution grid would lead to matrices too large to handle. We tested three resolutions to confirm that our resolution was good enough.

We not only need to properly resolve these averaging kernels, but we need to handle the truncation of the kernels to one hemisphere. Indeed, let us consider the cases of the averaging kernels computed for target locations nearly at the equator.<sup>5</sup> If we compute the center of gravity of  $K^{(a)}(r, \theta)$  for  $0 \leq \theta \leq \frac{\pi}{2}$  the resulting latitude of the center of gravity will be some positive relatively large value, yet because of the hemispherical symmetry of the problem, the averaging kernel of the symmetric solution is that symmetrized kernel. This skewness will, of course, extend to a range of low latitudes.

<sup>5</sup> Since we use piecewise constant functions for the discretization of the inverse problem, our lowest latitude, being effectively at the midpoint, will be half the latitude increment.

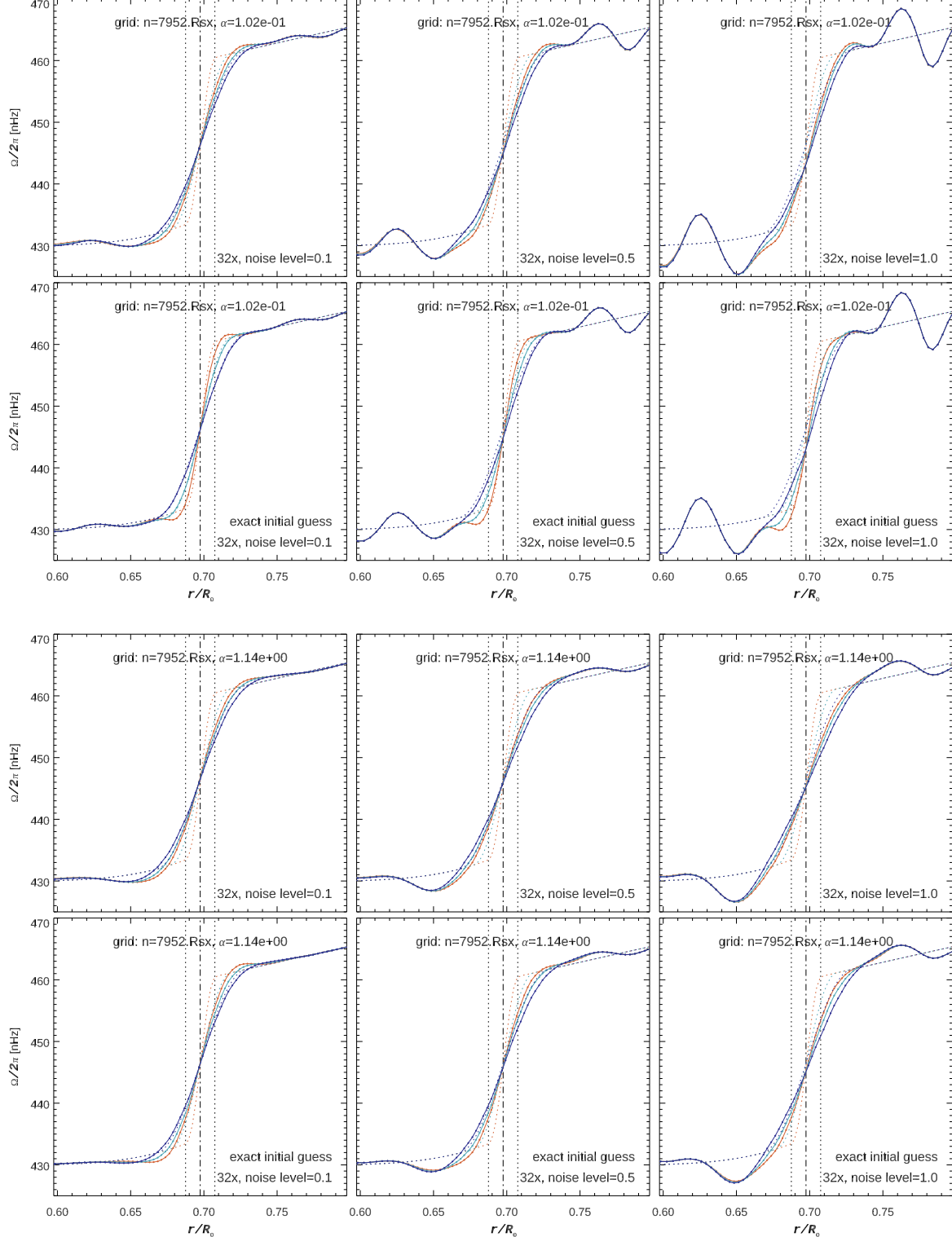


**Figure 9.** SART solutions for noisy simulations (solid lines with dots) superimposed over the true solutions (dashed lines) for the three models (shown with different colors), using the *progressive I* grid. The top two rows correspond to almost no smoothing, while the bottom two rows to “typical” smoothing (as per value of  $\alpha$ ). Rows alternate cases with constant or exact initial guess, while columns correspond to increasing levels of noise, with respect to the uncertainties resulting from fitting a  $32 \times 72$ d time series (from left to right).

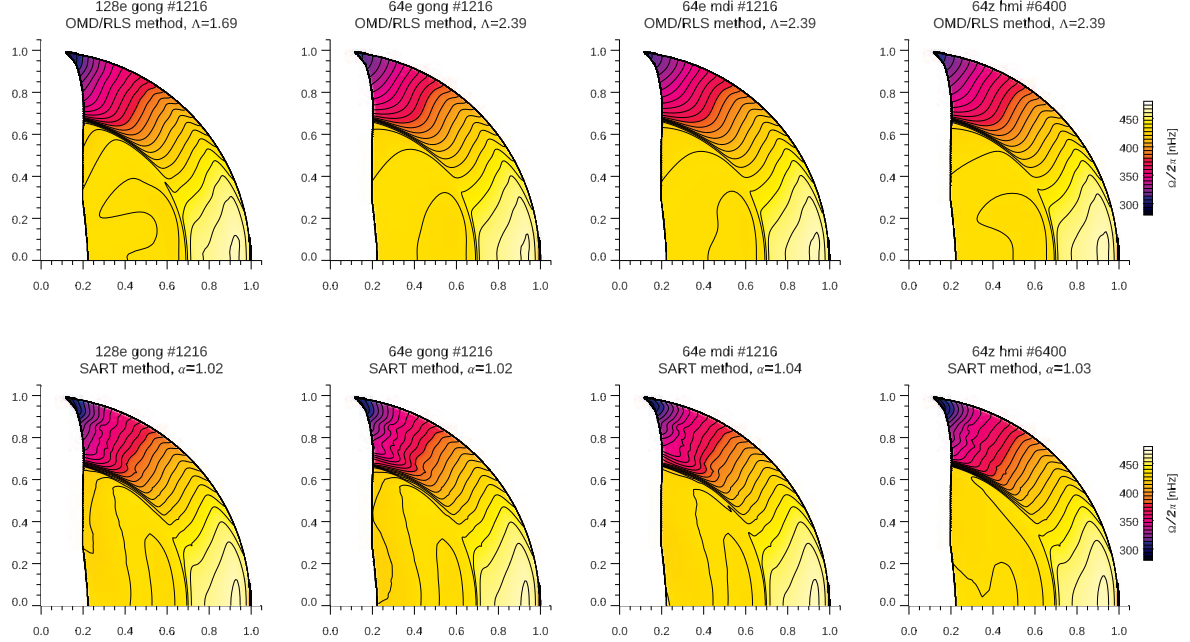


**Figure 10.** Inverted rotation rate derived from splittings resulting from fitting very long time series, i.e., 25.2 years of GONG observations (leftmost panel) and long time series, i.e., 12.6 years of GONG, MDI or HMI observations (rightmost 3 columns), using either RLS or SART inversion methodology (top versus bottom row).

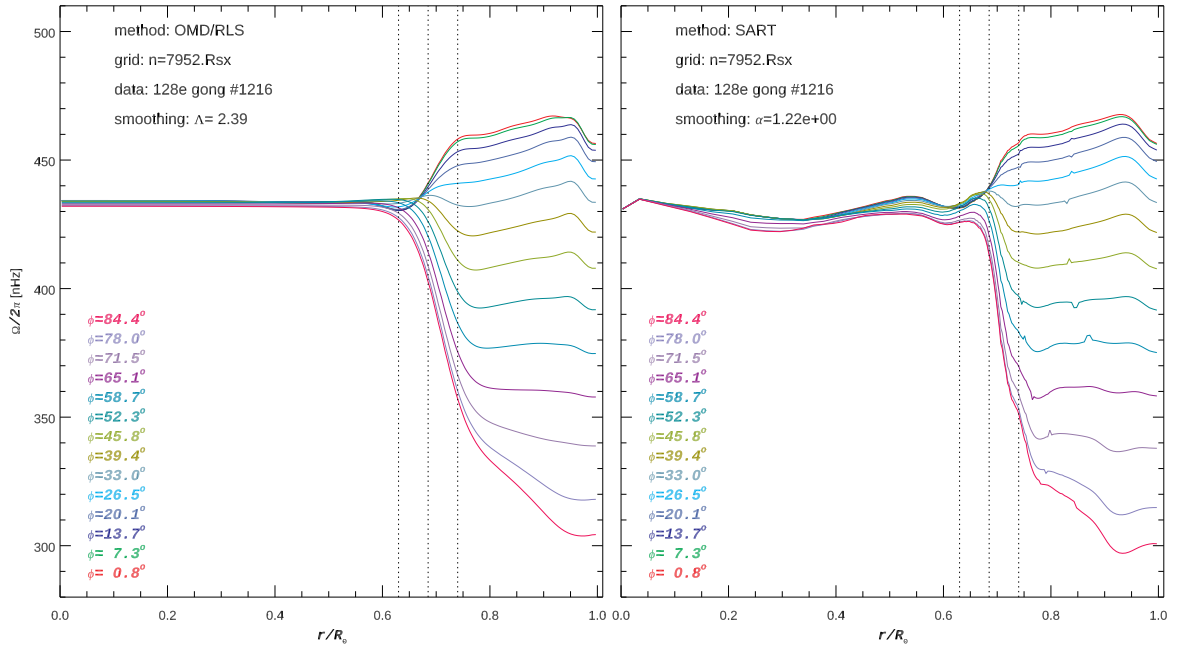


**Figure 11.** Inverted rotation rate derived from splittings resulting from fitting a very long time series, i.e., 25.2 years of GONG observations, plotted as a function of radius for a set of latitudes, using either the RLS or SART inversion methodology (left versus right panels).

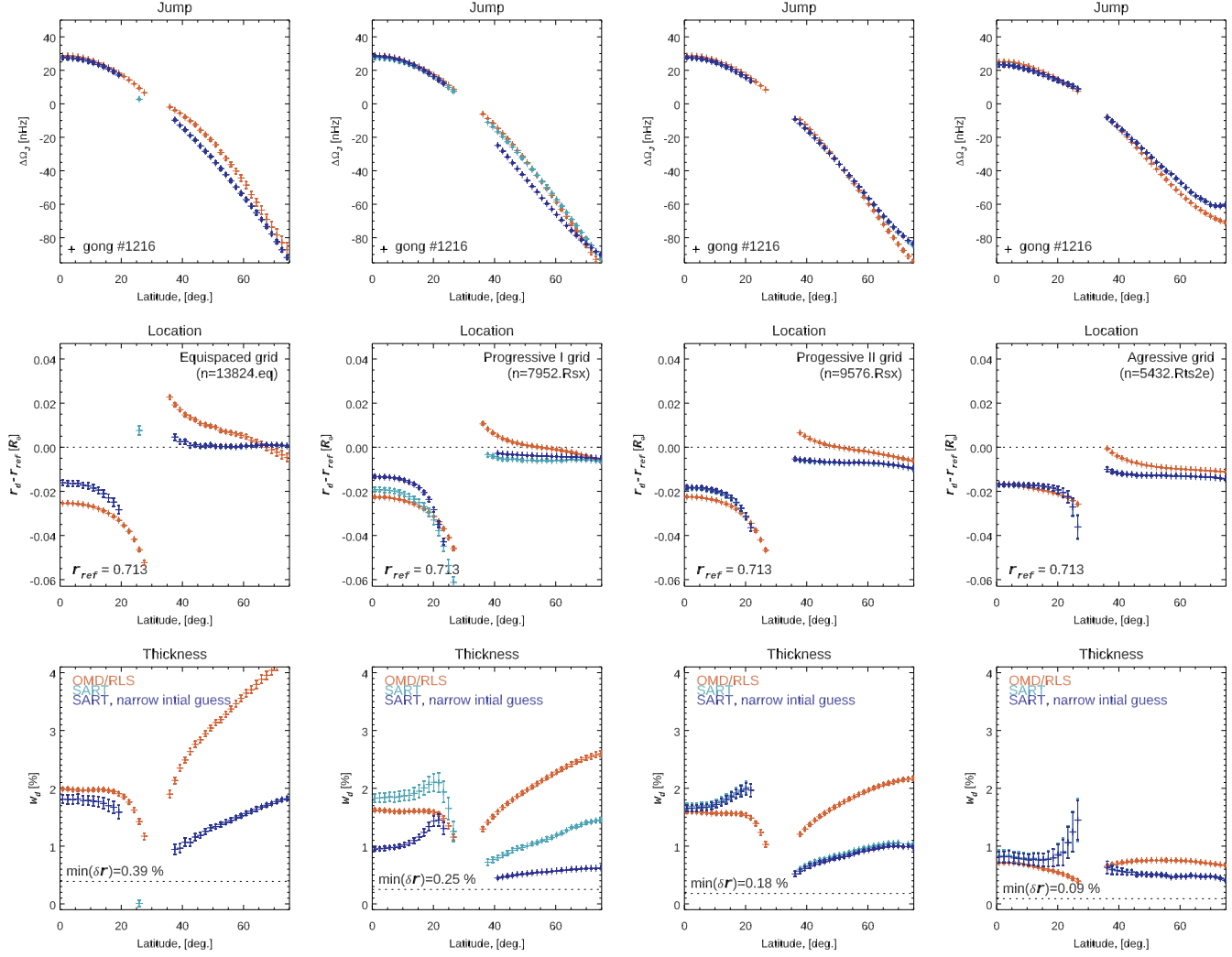


**Figure 12.** Characteristics of the tachocline resulting from fitting, around the tachocline, a sigmoid with two slopes to inverted rotation rates derived from splittings resulting from fitting a very long time series, i.e., 25.2 years of GONG observations. Namely, from top to bottom, the total jump,  $\Delta\Omega_J$ , location,  $r_d$ , and thickness,  $w_d$ , are plotted as a function of latitude, for inversions using the RLS and SART methods for, from left to right, four different inversion grids, i.e., an equispaced, two progressive and one aggressive radial density grid. The location is shown with respect to the base of the convection zone, i.e.,  $r = 0.713R_\odot$ , while, for comparison with the inferred widths, the resolution of the inversion grid at the tachocline is indicated by the horizontal dotted lines.

In order to mitigate this, we define and compute what we call extended averaging kernels, that cover the full  $-\frac{\pi}{2} \leq \theta \leq \frac{\pi}{2}$  range, and compute the center of gravity of this extended averaging kernel. This extension consists in assigning the values obtained at latitudes above the target latitude to values at negative latitudes, separated by the same distance from the target latitude, namely, for positive  $\theta$  we use

$$K_{i,j}^{(a_e)}(r, -\theta) = K_{i,j}^{(a)}(r, \theta + (\theta + \theta_j)) \quad (11)$$

for  $0 \leq 2\theta + \theta_j \leq \frac{\pi}{2}$ . Examples of extended averaging kernels are illustrated in Fig. 13 for three latitudes, one radius and three inversions grids.

This being said, we recognize that using the center of gravity, even from high resolution extended averaging kernels is most likely not the optimal way to determine the effective location of the derived solution. Yet it also shows how when using the aggressive grid this effective location is skewed by the averaging kernels. This is best illustrated by

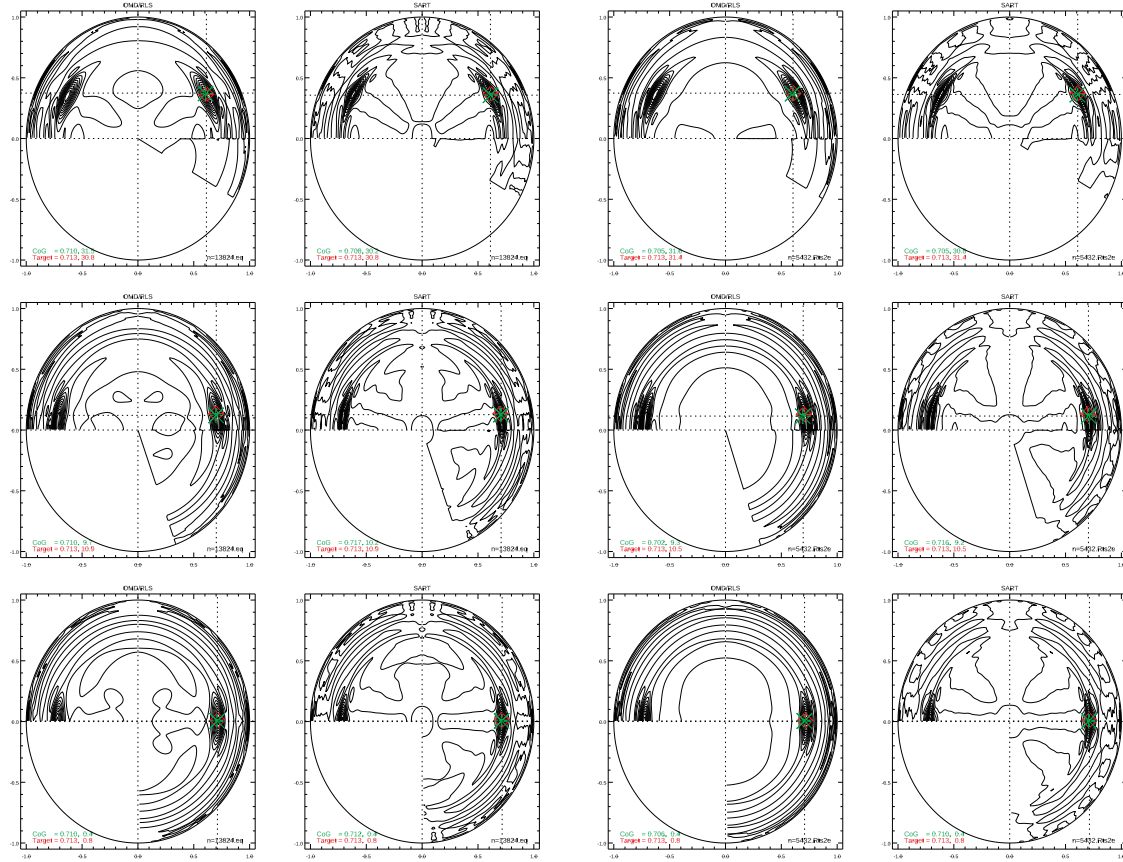


**Figure 13.** Illustration of the extended averaging kernels, for three latitudes (top to bottom) at  $r/R_\odot = 0.714$ , for two grids (equispaced and aggressive grids, columns) and both methods (even/odd columns). The averaging kernel is shown on the left, while the extended averaging kernels is shown on the right, with the 50% contour in bold. The target location is indicated in red while the center of gravity of the extended kernel is indicated in green.

the animations in Fig. 14, that show how, at some fixed latitude, the averaging kernels change as a function of radius around the tachocline, for different inversion grids and inversion methodologies.

These animations show how for the *aggressive* grid, the location of the averaging kernel, and hence its center of gravity, jumps around for the target locations near the tachocline where the radial density is very high. In fact the center of gravity, indicated by the blue symbol, loops around the target location. This effect is more pronounced when using the RLS method, but disappears when using the *progressive* or *equispaced* grids for either inversion technique.

With this caveat in mind, we remapped the rotation rate on the center of gravity of the extended high resolution averaging kernels and fitted our sigmoid model. The resulting parameters are shown in Fig. 15, and yet despite some small changes in the resulting estimates, the main characteristic of these estimates remains unchanged, including the discontinuity of the tachocline location,  $r_d$ .

Next, we plot on Fig. 16, the tachocline location and width (i.e., the FWHJ) derived from three inversions (RLS, SART and SART with narrow initial guess, all remapped on the effective locations, using one of the progressive radial density grids) and compare them to other estimates. Namely to the equatorial values tabulated in Table 2, but also to the values reported by Basu & Antia (2003) and more recently by Basu et al. (2024), values computed using forward modeling of the splitting expansion coefficients. Basu & Antia (2003) used one and two-dimensional rotation models and the respective projects pipeline results (GONG and MDI) derived from fitting 108 or 72 day long time series. The plotted values are the average values computed from the non-overlapping GONG and MDI data set spanning the 1995 to 2002 interval. The more recent Basu et al. (2024) results are based on splitting estimated from much longer time series (Korzennik 2023) but uses a one dimensional rotation model, hence produced equatorial estimates, although

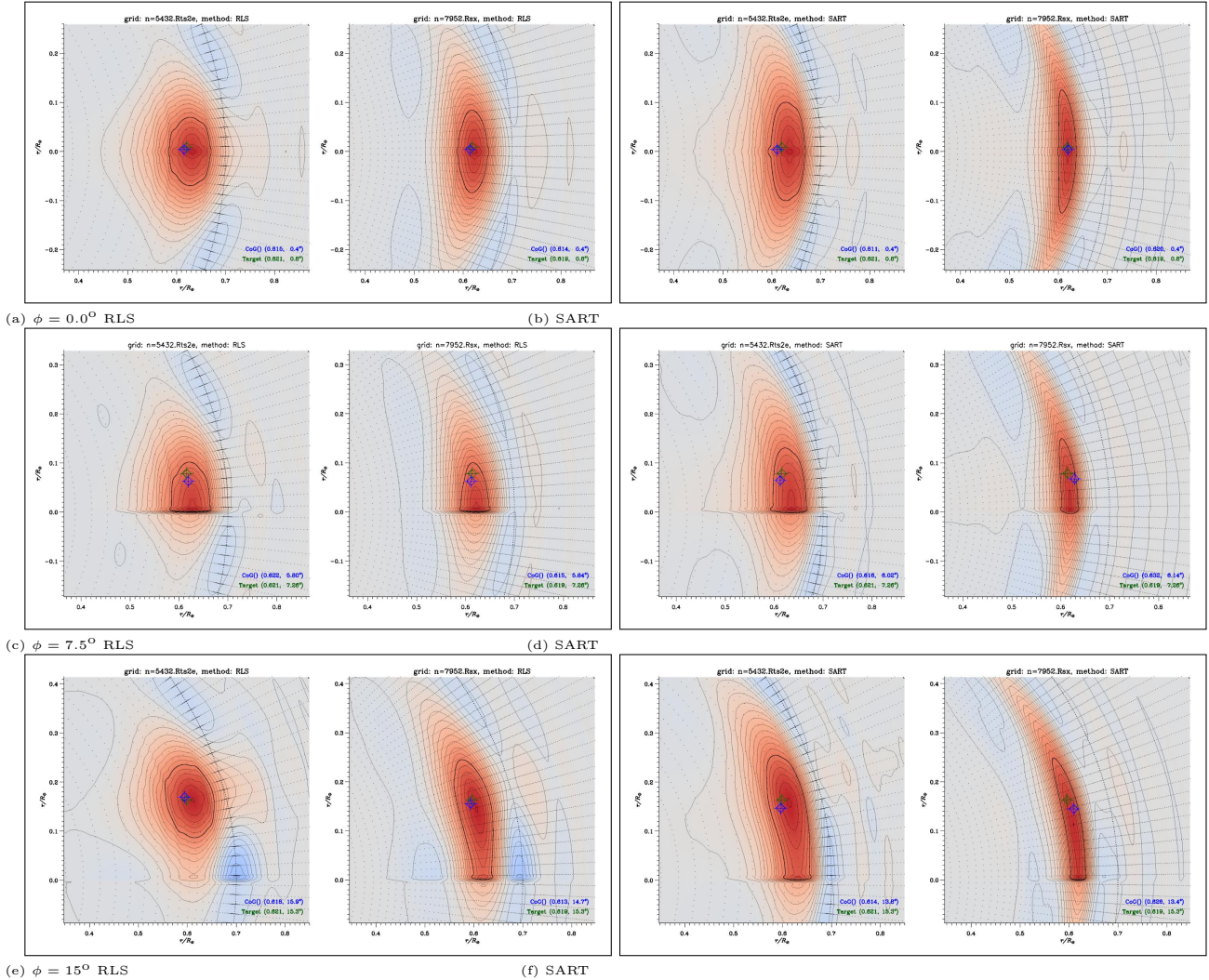


**Figure 14.** Animations of average kernels at three latitudes ( $\phi = 0, 7.5 \& 15^\circ$ ), for two grids and two inversion methodologies. The animations show the evolution of the average kernels as the target radius changes, comparing the *aggressive* with the *progressive I* grid (left versus right panels). Notice how the average kernel is “jumping” as the target radius crosses the tachocline when using the *aggressive* grid, but not the *progressive* one.

effectively these estimates correspond to some average over a range of latitudes around the equator (indicated by the latitudinal extent of the corresponding horizontal lines).

This forward modeling, derived from the same splittings, has since been expanded to either a one dimensional model at various latitudes or a two-dimensional model of the tachocline using a polynomial expansion with 2, 3 or 4 terms for the latitudinal variation of  $r_d$  (Basu and Korzennik 2025). Results from that work are also indicated on Fig. 16. Note that the formal uncertainties on the tachocline characteristics derived from fitting a sigmoid model to inversion inferences are bound to be small, since the inversion profile itself is a smoothed estimate of the true underlying rotation profile.

Note the remarkable agreement between most methods, although using a polynomial expansion for the forward modeling dependence on latitude cannot reproduce the discontinuity seen in our two-dimensional inversions. Attempts to carry out forward modeling with more terms or by including a discontinuity has so far produced worse models with excessively large uncertainties at high latitudes (see Basu and Korzennik 2025).

Another way to look at the location of the tachocline is to compute the rotation rate gradient, and visualize its amplitude, namely  $|\nabla\Omega|$ . Fig. 17 shows the amplitude of this gradient and compares it to the location of the tachocline derived from estimates of  $r_d$ . These estimates match the location of the maximum gradient and while the gradient

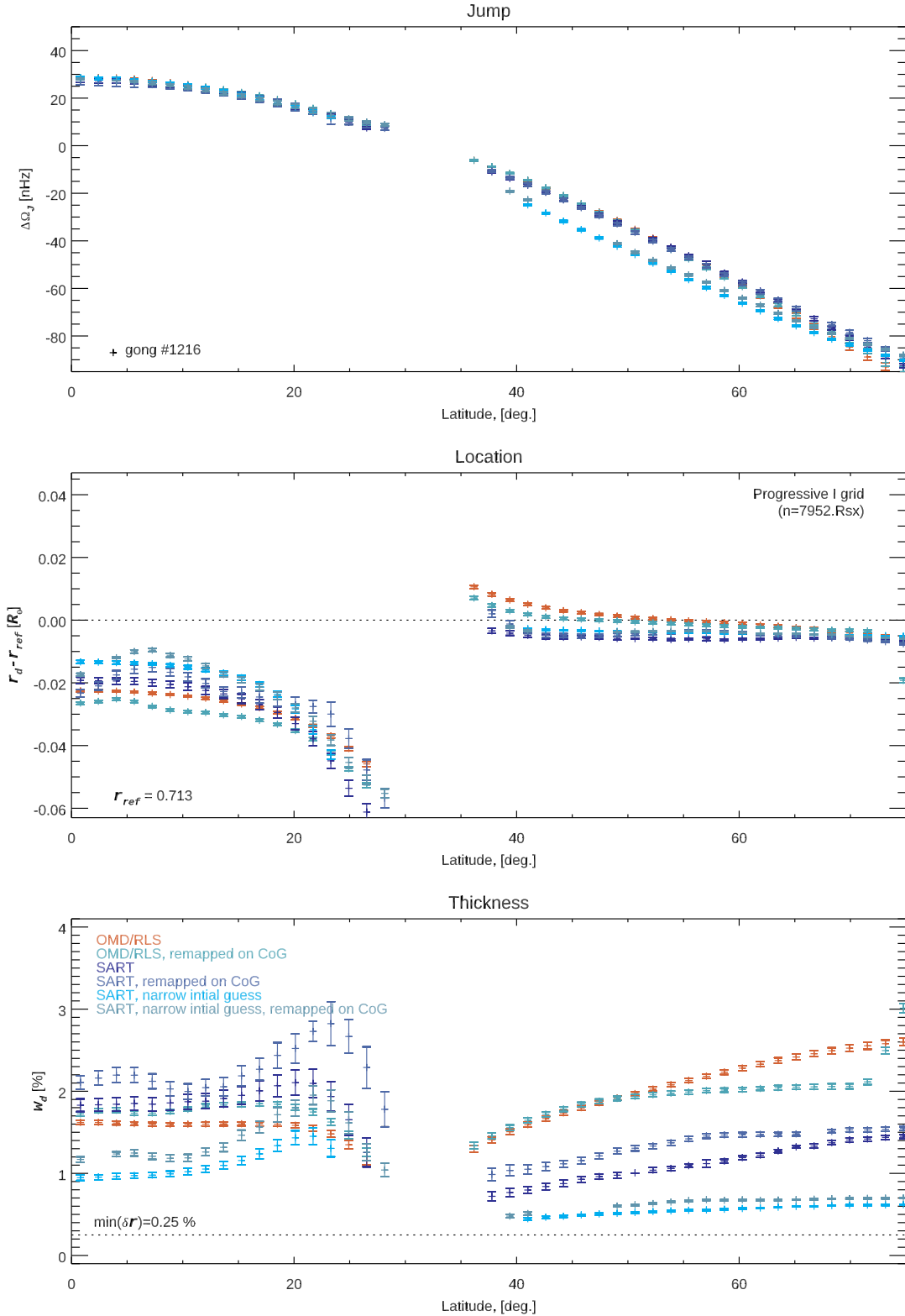


**Figure 15.** Characteristics of the tachocline resulting from fitting a sigmoid to inverted rotation rates derived from fitting a very long time series, i.e., 25.2 year of GONG observations, plotted as a function of latitude, after remapping the rotation rate on the center of gravity of extended high resolution average kernels, or not. It shows that the remapping affects mostly our estimates of the tachocline thickness, the parameter most difficult to constrain, but does not significantly change our estimates of its position.

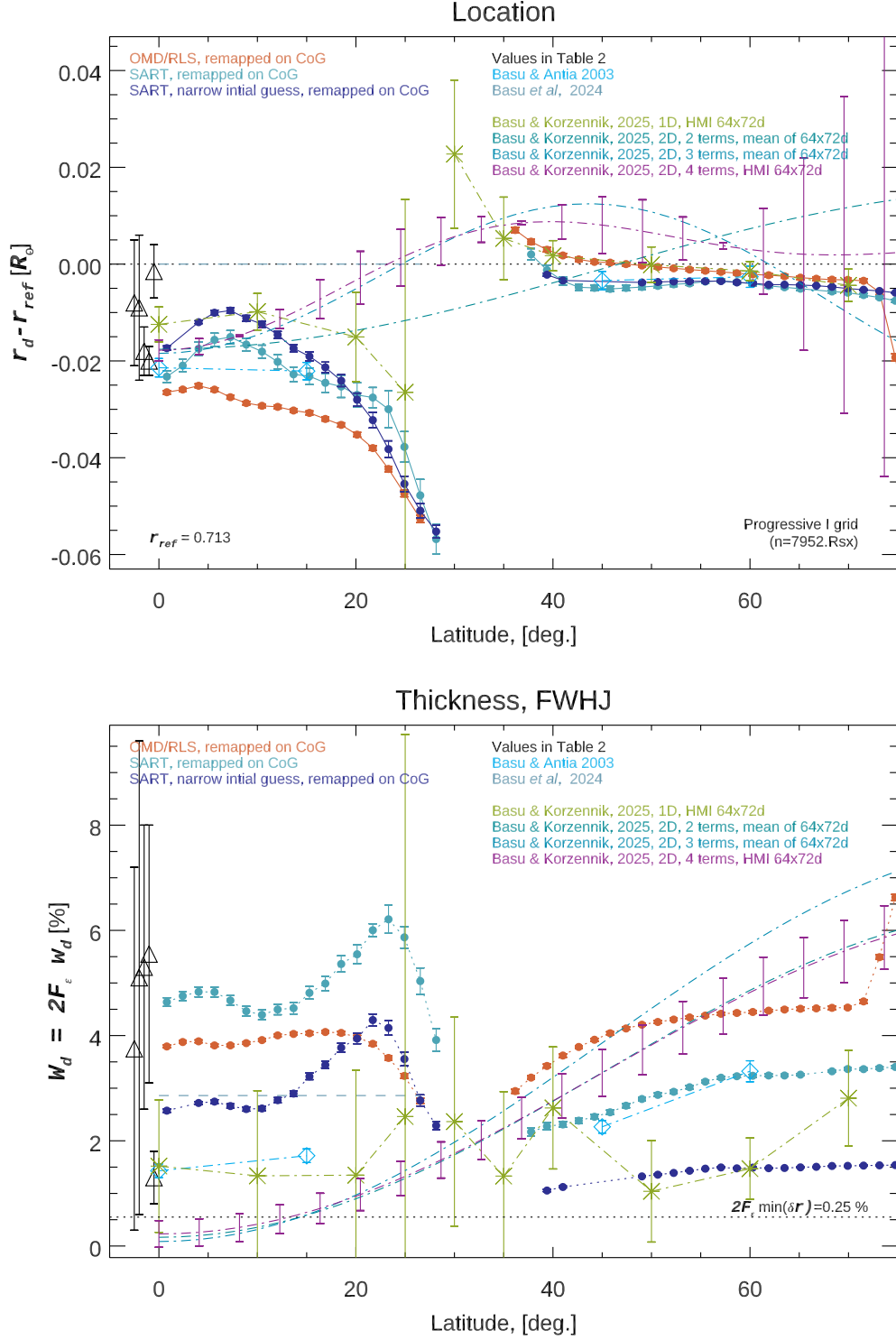


**Figure 16.** Characteristics of the tachocline, i.e., position and FWHJ, as a function of latitude resulting from fitting a sigmoid to inverted rotation rates derived from fitting a very long time series, i.e., 25.2 year of GONG observations (filled circles), for three cases (see legend). These are compared to the equatorial values in Table 2 (black triangles, offset to negative latitudes for clarity) and to values estimated using a forward modeling technique, from Basu & Antia (2003) (diamonds), from the more recent Basu et al. (2024) (horizontal dash line). It also shows results from (Basu and Korzennik 2025), whether using a one dimensional or a two-dimensional model (star vs. dot-dash lines), and for the latter whether using 2, 3 or 4 terms in the polynomial expansion of  $r_t$  (see legend and Basu and Korzennik 2025, for additional details).

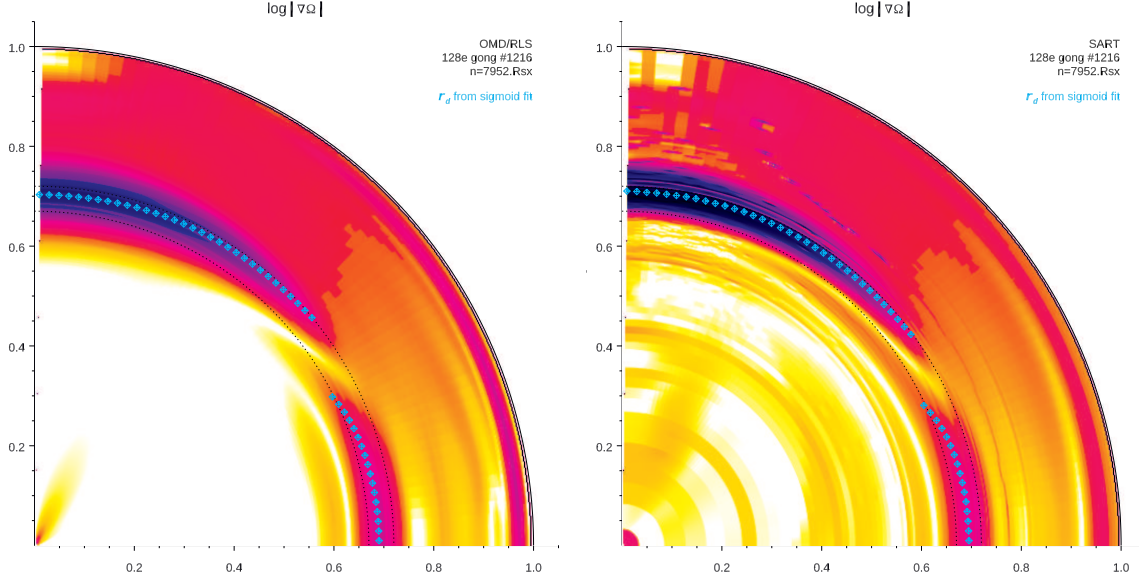


**Figure 17.** Amplitude of the rotation rate gradient,  $|\nabla\Omega|$ , resulting from inverting splittings derived from a very long time series and using either inversion methodology (left versus right panel). The gradient is shown on a logarithmic scale and the position of the jump location,  $r_d$ , measured by fitting a sigmoid is shown as well (crosses).

derived using the SART methodology is more noisy, the visualization of the gradient shows clearly the duality of the location of the tachocline, curving inwards with latitude at low latitudes only to reappear at larger radii at the higher latitudes.

#### 5.4. Tachocline Characteristics Using Long Time Series

We also inverted the splittings resulting from fitting somewhat shorter time series, namely 12.6 and 6.3 year long observations of GONG, MDI and HMI. Our sigmoid model was then fitted to the inferred rotation rates. Since fitting shorter time series leads to larger uncertainties, the smoothing was somewhat increased in each case compared to the smoothing used for the very long time series.

Figs. 18 and 19 show the resulting tachocline characteristics, when using either inversion method on each available data set. While each method returns slightly different values, especially at higher latitudes, the discontinuity of the location of the tachocline is consistently observed for each data set. Not surprisingly the RLS method returns a wider tachocline at high latitudes, something that we attribute to the method greater smoothing. The mean characteristics, derived from averaging over the data sets, are also plotted in these figures and are consistent with each other and the corresponding characteristics derived from the very long time series.

Temporal changes of either the tachocline jump amplitude, location, or width derived from fitting a sigmoid model to inversion results, even when averaged over either low or high latitudes (i.e., for  $\phi \leq 30^\circ$  or for  $35^\circ \leq \phi \leq 60^\circ$ ), remain quite noisy, as shown in Fig. 20. Despite the latitudinal averaging there is no definite or significant temporal variation, although the scatter and the formal error bars are somewhat smaller for inferences using the RLS inversion methodology. At low latitudes these means indicate a possible decrease of the jump amplitude by about 1 nHz around 2006, a trend that is not quite compatible with the changes inferred in Basu et al. (2024), where such decrease peaks around 2002. These also suggest a correlated small change in the location, i.e., a tachocline located a little deeper, by  $\sim 0.005R_\odot$ , when the amplitude of the jump is smaller. The figure also shows a marginal decrease of the mean width with time at low latitudes, but the same characteristics derived when using the SART method (jump, position and width), although more scattered and noisy, do not align with the RLS method results. At high latitudes, the inferred jump amplitude appears to also change with time, but here again the changes are method dependent although more pronounced. These systematic differences are most likely the result of the different amount of effective smoothing of each method, especially at high latitude.

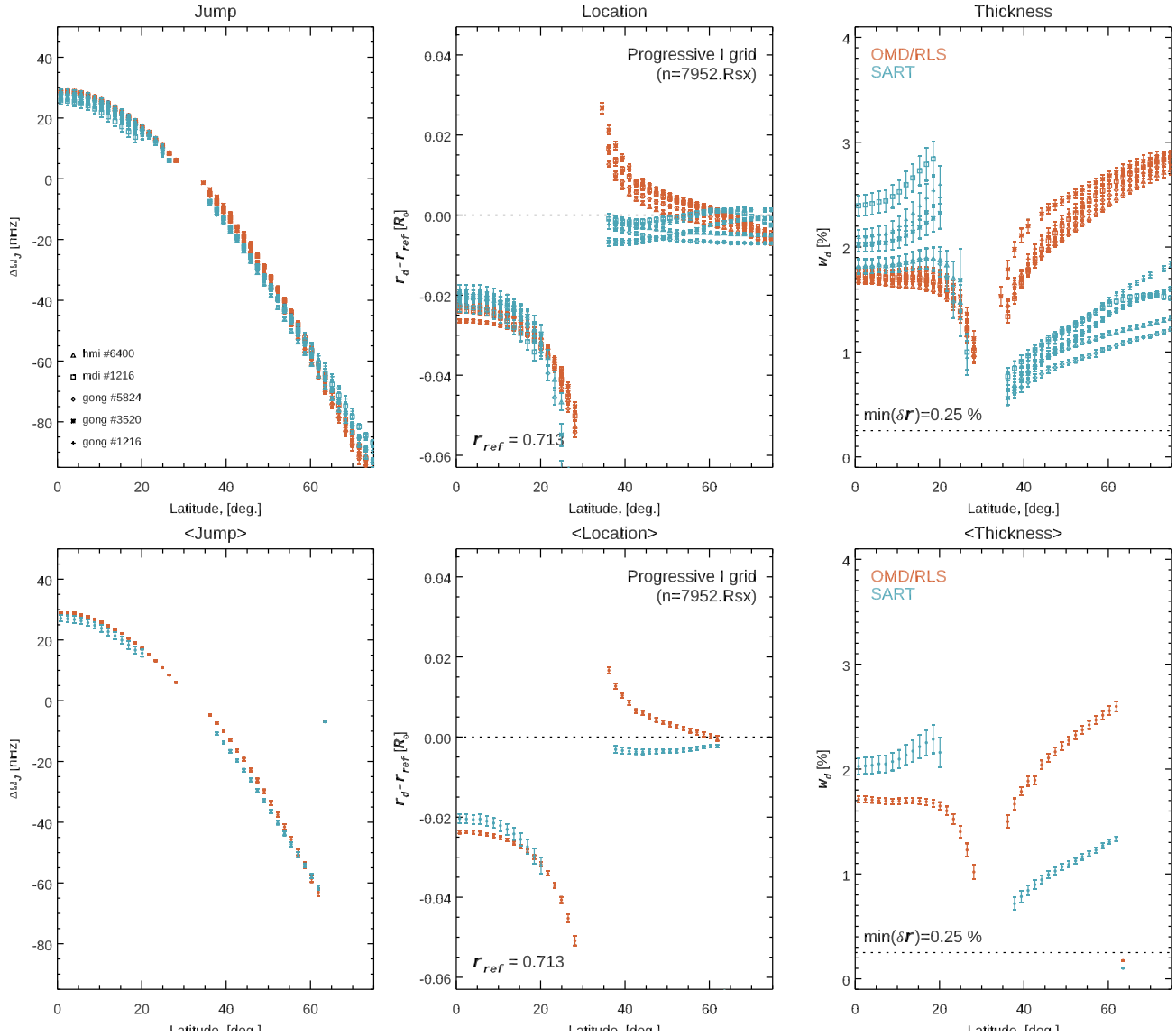


**Figure 18.** Top panels: characteristics of the tachocline resulting from fitting a sigmoid to inverted rotation rates derived from fitting a 12.6 year-long time series of GONG, MDI and HMI observations, i.e., six sets of splittings and both methodologies. The jump, location and width are plotted as a function of latitude, with colors indicating the inversion method, while the different symbols correspond to the different splittings sets. The bottom panels show, for each method, the mean jump, location and width plotted as a function of latitude, with colors indicating the inversion method.

## 6. CONCLUSIONS

Using very long and long time series, we have carried out rotation inversions using two different methodologies. Since we wanted to characterize the tachocline we have first shown how each method performs when adjusting the inversion grid, especially in the radial direction around the tachocline and when fine tuning each method's smoothing and trade-off. To do this we used simulations without and with random noise. We conclude from this that one should not use an aggressive radial grid, i.e., a grid that becomes very dense *only* around the tachocline, as it produces artifacts, especially once noise is included. Yet, using a radial grid with a progressive transition of its radial density mitigates most of these artifacts, although it requires more computing resources, especially if one aims to reach a very high radial resolution at the tachocline. We also have shown that one can improve the inferences of the SART

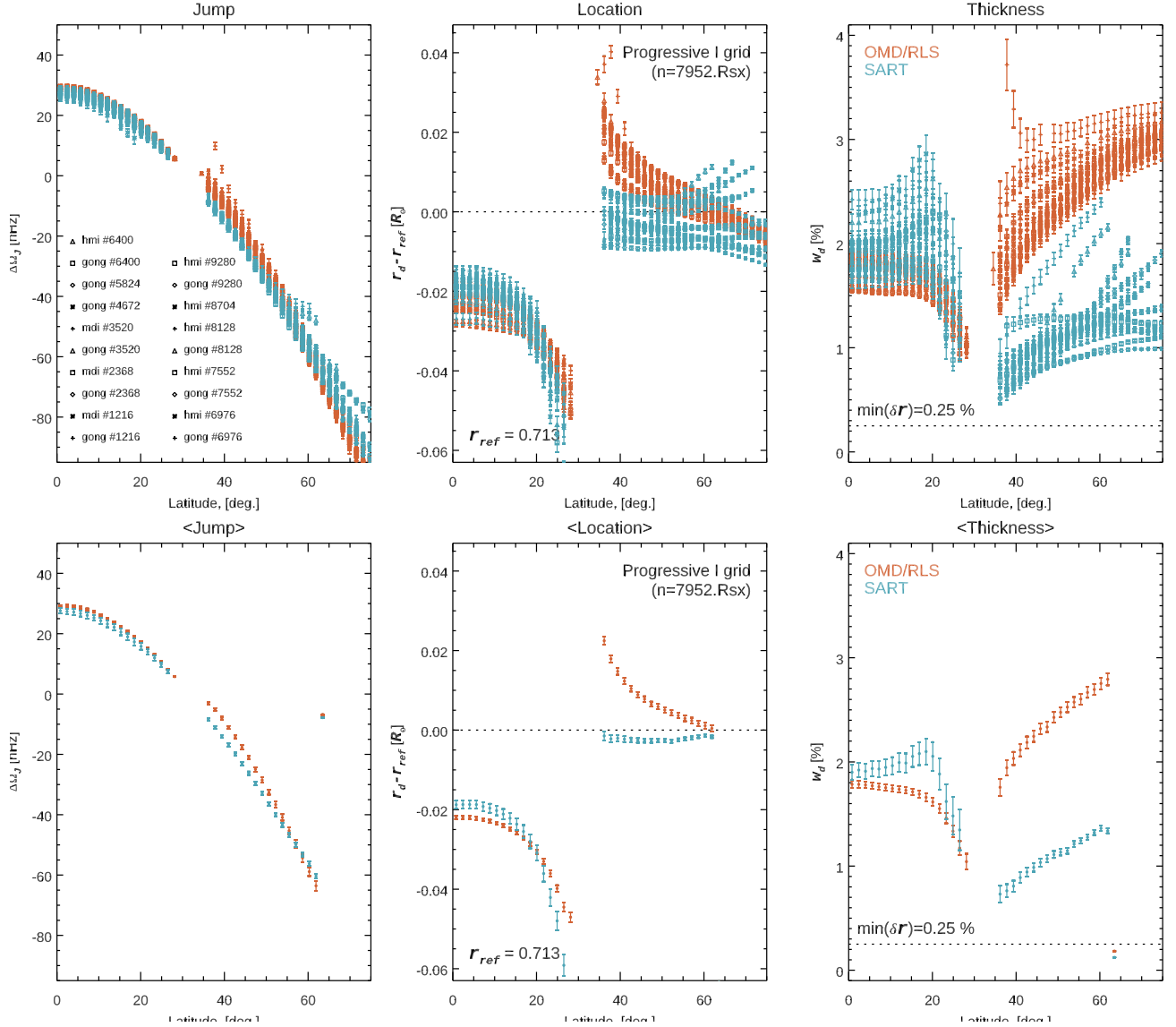


**Figure 19.** Top panels: characteristics of the tachocline resulting from fitting a sigmoid to inverted rotation rates derived from fitting a 6.3 year-long time series of GONG, MDI and HMI observations, i.e., 19 sets of splittings and both methodologies. The jump, location and width are plotted as a function of latitude, with colors indicating the inversion method, while the different symbols correspond to the different splittings sets. The bottom panels show, for each method, the mean jump, location and width plotted as a function of latitude, with colors indicating the inversion method.

method by using an initial guess derived from the RLS solution, although fine tuning both the way that initial guess is constructed (i.e., sharpened) and the precise smoothing parametrization of the SART method remains delicate.

By fitting a sigmoid model of the tachocline to our inverted profiles we inferred the variation with latitude of the rotation radial shear, i.e., the amplitude of the rotation rate jump across the tachocline, the location of this shear and an estimate of the width of the tachocline.

We find that the location of the tachocline does not vary smoothly with latitude, but instead shows a clear discontinuity between its position at low latitudes, where the radial shear is positive, and its position at high latitudes, where that shear is negative. This is also clearly seen when looking at the rotation rate gradient and persists when using splittings derived from somewhat shorter time series and when using either inversion methodology.

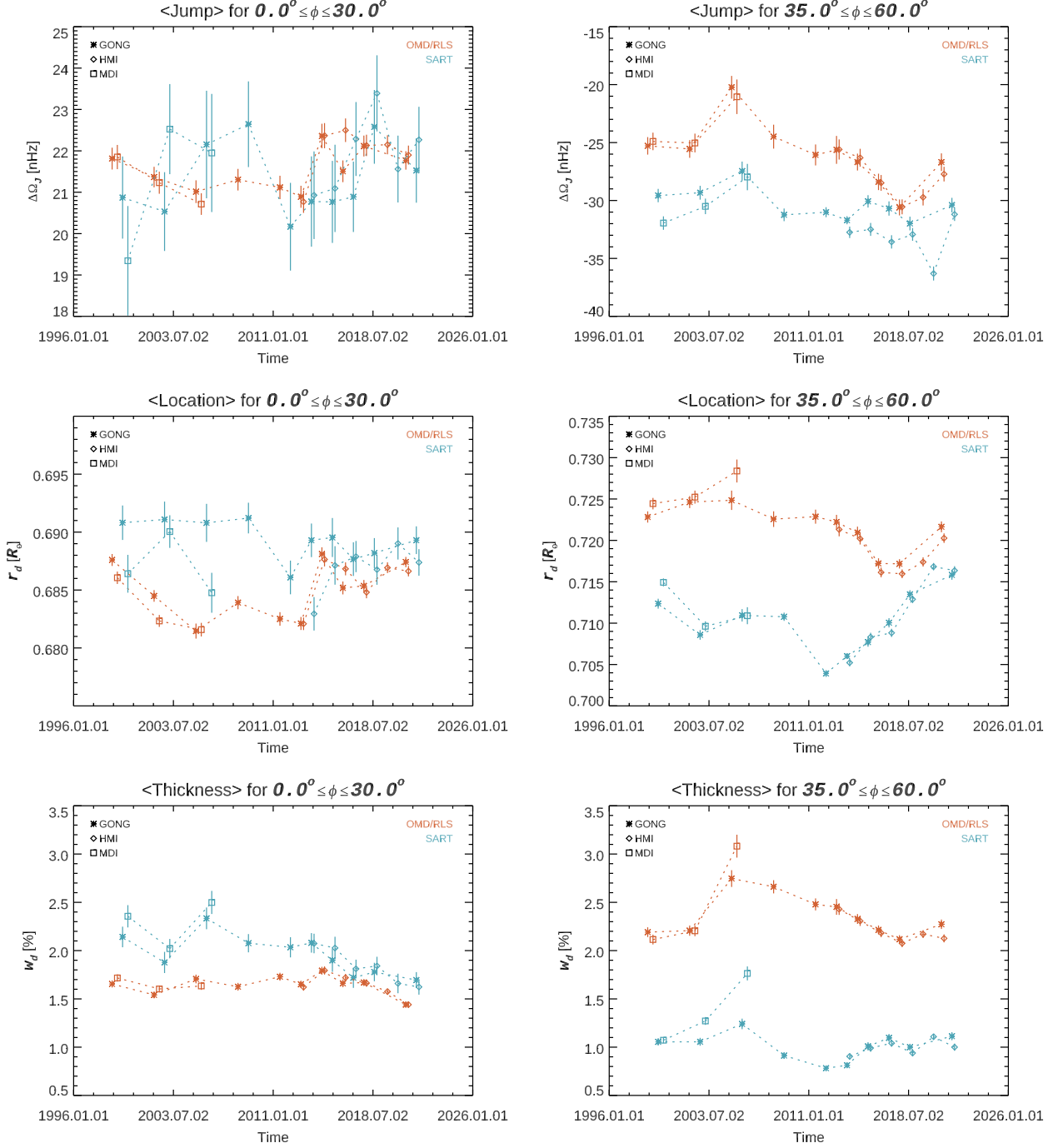


**Figure 20.** Characteristics of the tachocline resulting from fitting a sigmoid to inverted rotation rates derived from fitting a 6.3 year-long time series of GONG, MDI and HMI observations, i.e., 19 sets of splittings, using either inversion methodology. These were averaged over two ranges in latitude and plotted as a function of time. The colors correspond to the inversion method, while the different symbols correspond to the different data sets (GONG, MDI, HMI). The panels on the left show the mean values for low latitudes ( $\phi \leq 30^\circ$ ), while the panels on the right show the mean values for high latitudes ( $40^\circ \leq \phi \leq 70^\circ$ ). These results are too noisy to detect a definite or significant temporal variation, although some trends with time are present.

Also, our estimates of the position and its variation with latitude match rather well estimates based on forward modeling using rotational splitting coefficients as in [Basu & Antia \(2003\)](#); [Basu et al. \(2024\)](#) and figures 5 & 6 of the more recent [Basu and Korzennik \(2025\)](#). Of course the discontinuity cannot be seen when such modeling uses a polynomial expansion of the tachocline characteristics with respect to latitude. We find that the tachocline lies below the convection zone, by  $0.02R_{\odot}$ , at low latitudes ( $\phi \leq 30^\circ$ ) only to coincide with the convection zone at the higher latitudes, once the radial shear is negative.

While we have made every effort to eliminate the possibility that the bifurcation we observe in the tachocline could be an inversion artifact, i.e., the result from limited latitudinal resolution, kernel geometry, or fitting degeneracies, especially when the jump amplitude becomes small, this is a new paradigm for the shape of the tachocline and thus would benefit from independent confirmation. Not surprisingly, we found no modeling of the tachocline that would produce or explain such bifurcation.

Our estimate of the tachocline width is commensurable with previous estimates and suggests that its FWHJ might be as low as 1% of the solar radius, if not lower since rotation inversion inferences are limited by the resolution of the averaging kernels. Estimates of this width when using a narrow initial guess for the SART case could be biased were the data a lot more accurate, hence allowing for much less smoothing. The values derived are overall in good agreement with the values derived by others, including [Basu and Korzennik \(2025\)](#), as shown in Fig. 16, despite the scatter. Yet, our inferences of its variation with latitude are still very method dependent, hence we cannot ascertain whether it really increases with latitude, as seen in inferences from forward modeling, although recent work using forward modeling of rotational splittings coefficients, using long time series of GONG observations (720-day long) and two different mode fitting pipe-lines show similar trends [Basu et al. \(submitted\)](#) Also, our estimate of the variation of the amplitude of the radial shear with latitude agrees rather well with corresponding estimates derived from forward modeling.

We introduced the concept of the extended averaging kernel, since we checked that our inferences of the tachocline characteristics were not an artifact of the variation of the effective position of the inferred rotation rate. Indeed, inversion inferences are a smoothed representation of the underlying *true* rotation rate, although we must add that the complex nature of the averaging kernel makes it tricky to derive an effective position.

As for changes with time, hence solar activity, we find that our current rotation inversion implementations remain too noisy to see definitive and significant temporal variations. We recognize that there remain systematic differences when using different methodologies. These method-dependent systematics currently dominate the resulting temporal variations, especially at high latitudes. We plan to further improve this by devising a more objective selection of the amount of smoothing and inversion trade off between resolution and error magnification for both methods.

## ACKNOWLEDGEMENTS

This work was partially supported by NASA grants 80NSSC22K0516 and NNN18ZDA001N-DRIVE to SGK and by the Spanish AEI programs ID2022-139159NB-I00 (Volca-Motion) and PID2022-140483NB-C21 (HARMONI) to AED.

## REFERENCES

Anderson, A. H., & Kak, A. C.: 1984, *Ultrasonic Imaging* **6**, 81. doi:10.1016/0161-7346(84)90008-7

Basu, S., Korzennik, S. G., and Tripathy, S. C. 2026, submitted to ApJ

Basu, S., Andrade de Aguiar, W. A. M., & Korzennik, S. G. 2024, ApJ, 975, 2, 276. doi:10.3847/1538-4357/ad82e6

Basu, S. & Korzennik, S. G. 2025, ApJ, 995, 1, 91. doi:10.3847/1538-4357/ae1cc6

Eff-Darwich, A. & Pérez Hernández, F. 1997, A&AS, 125, 391. doi:10.1051/aas:1997229

Eff-Darwich, A., Korzennik, S. G., & García, R. A. 2010, Astronomische Nachrichten, **331**, 890. doi:10.1002/asna.201011420

Hansen, C., Cox, J., and van Horn, H.: 1977, ApJ, **217**, 151.

Korzennik, S.G.: 2023, *Frontiers in Astronomy and Space Sciences* **9**, 1031313. doi:10.3389/fspas.2022.1031313.

Korzennik, S. G. & Eff-Darwich, A. 2024, SoPh, 299, 6, 86. doi:10.1007/s11207-024-02334-7

van der Sluis, A., and van der Vorst, H.A.: 1990, *Linear Algebra and its Applications*, **130**, 257.

Antia, H.M., Basu, S., and Chitre, S.M.: 1998, *Monthly Notices of the Royal Astronomical Society*, **298**, 543–551.

Balbus, S.A., and Weiss, N.O.: 2010, In: Hasan, S.S. and Rutten, R.J. (eds.), *Magnetic Coupling Between the Interior and the Atmosphere of the Sun*, Springer-Verlag, Berlin, p. 53.

Basu, S., and Antia, H.M.: 2003, *The Astrophysical Journal*, **585**, 553–565.

Basu, S., and Antia, H.M.: 2019, *The Astrophysical Journal*, **883**(1), 93.

Basu, S., Andrade de Aguiar, W.A.M., and Korzennik, S.G.: 2024, *The Astrophysical Journal*, **975**, 276.

Brun, A.S., Miesch, M.S., and Toomre, J.: 2011, *The Astrophysical Journal*, **742**, 79.

Buldgen, G., Salmon, S.J.A.J., Godart, M., et al.: 2017, *Monthly Notices of the Royal Astronomical Society*, **472**, L70–L74.

Caleo, A., Balbus, S.A., and Potter, W.J.: 2015, *Monthly Notices of the Royal Astronomical Society*, **446**, 1–8.

Canuto, V.M.: 1998, *The Astrophysical Journal*, **497**, L51–L54.

Charbonneau, P., Christensen-Dalsgaard, J., Henning, R., et al.: 1999, *The Astrophysical Journal*, **527**, 445–460.

Corbard, T., Berthomieu, G., Provost, J., and Morel, P.: 1998, *Astronomy and Astrophysics*, **330**, 1149–1159.

Corbard, T., Blanc-Féraud, L., Berthomieu, G., and Provost, J.: 1999, *Astronomy and Astrophysics*, **344**, 696–708.

Christensen-Dalsgaard, J.: 2018, *Monthly Notices of the Royal Astronomical Society*, **478**, L77–L81.

Dikpati, M., and Gilman, P.A.: 2006, *Advances in Space Research*, **38**, 845–855.

Elliott, J.R., and Gough, D.O.: 1999, *The Astrophysical Journal*, **516**, 475–484.

Elliott, J.R.: 1997, *Astronomy and Astrophysics* **327**, 1222.

Forgács-Dajka, E., and Petrovay, K.: 2001, *Solar Physics*, **203**, 195–206.

Garaud, P., and Garaud, J.-D.: 2008, *Monthly Notices of the Royal Astronomical Society*, **387**, 4189–4209.

Gilman, P.A.: 2018, *The Astrophysical Journal*, **853**, 65.

Gough, D.O., and McIntyre, M.E.: 1998, *Nature*, **394**, 755–759.

Howe, R., Christensen-Dalsgaard, J., Hill, F., et al.: 2000, *The Astrophysical Journal Letters*, **533**, L163–L166.

Howe, R.: 2009, *Living Reviews in Solar Physics*, **6**(1), 1.

Howe, R.: 2020, In: Monteiro, M.J.P.F.G., García, R.A., Christensen-Dalsgaard, J., and McIntosh, S.W. (eds.), *Dynamics of the Sun and Stars*, Springer Nature Switzerland AG, pp. 71–74.

Jain, K., Jain, N., Tripathy, S.C., and Dikpati, M.: 2022, *The Astrophysical Journal*, **925**, 41.

Jørgensen, A.C.S., and Weiss, A.: 2018, *Monthly Notices of the Royal Astronomical Society*, **472**, L70–L74.

Kagan, D., and Arras, P.: 2015, *The Astrophysical Journal*, **809**, 137.

Kim, E.J.: 2005, *Astronomy and Astrophysics*, **441**, 763–772.

Kim, E.J., and Leprovost, N.: 2007, *Astronomy and Astrophysics*, **468**, 1025–1031.

Kosovichev, A.G.: 1996, *The Astrophysical Journal Letters*, **469**, L61–L64.

Noone Wade, J.B., and Brummell, N.: 2020, In: Monteiro, M.J.P.F.G., García, R.A., Christensen-Dalsgaard, J., and McIntosh, S.W. (eds.), *Dynamics of the Sun and Stars*, Springer Nature Switzerland AG, pp. 201–204.

Ossendrijver, M.: 2003, *Astronomy and Astrophysics Review*, **11**, 287–364.

Rajaguru, S.P., and Antia, H.M.: 2015, *The Astrophysical Journal*, **813**, 114.

Rajaguru, S.P., and Antia, H.M.: 2020, In: Monteiro, M.J.P.F.G., García, R.A., Christensen-Dalsgaard, J., and McIntosh, S.W. (eds.), *Dynamics of the Sun and Stars*, Springer Nature Switzerland AG, pp. 107–118.

Rempel, M.: 2005, *The Astrophysical Journal*, **622**, 1320–1330.

Russell, C.T., Luhmann, J.G., and Jian, L.K.: 2019, *Reviews of Geophysics*, **57**(4), e2019RG000645.

Schou, J., Christensen-Dalsgaard, J., and Thompson, M.J.: 1994, *The Astrophysical Journal*, **433**, 389–401.

Schou, J., Antia, H.M., Basu, S., et al.: 1998, *The Astrophysical Journal*, **505**, 390–414.

Strugarek, A., Belucz, B., Brun, A.S., et al.: 2023, *Living Reviews in Solar Physics*, preprint submitted for review.

Takata, M., and Shibahashi, H.: 2003, *Publications of the Astronomical Society of Japan*, **55**, 1013–1022.

Vasil, G.M., Lecoanet, D., Burns, K.J., et al.: 2024, *Nature Physics*, **20**, 429–436.

Antia, H.M. and Basu, S.: 2011, *The Astrophysical Journal*, **735**, L45. doi:10.1088/2041-8205/735/2/L45.

de Jager, C., Akasofu, S.-I., Duhau, S., Livingston, W.C., Nieuwenhuijzen, H., and Potgieter, M.S.: 2016, *Space Science Reviews* **201**, 109. doi:10.1007/s11214-016-0293-9.

Howe, R.: 2020, *Dynamics of the Sun and Stars; Honoring the Life and Work of Michael J. Thompson* **57**, 63. doi:10.1007/978-3-030-55336-4\_8.

Weiss, N.O. and Thompson, M.J.: 2009, *Space Science Reviews* **144**, 53. doi:10.1007/s11214-008-9435-z.

Basu, S.: 1997, *Monthly Notices of the Royal Astronomical Society* **288**, 572. doi:10.1093/mnras/288.3.572.

Wilson, P.R., Burtonclay, D., and Li, Y.: 1996, *The Astrophysical Journal* **470**, 621. doi:10.1086/177893.

Charbonneau, P. and Tomczyk, S.: 1997, *Computational Astrophysics; 12th Kingston Meeting on Theoretical Astrophysics* **12**, 49.

Basu, S. and Antia, H.M.: 2001, *Monthly Notices of the Royal Astronomical Society* **324**, 498. doi:10.1046/j.1365-8711.2001.04364.x.

Basu, S. and Antia, H.M.: 2003, *The Astrophysical Journal* **585**, 553. doi:10.1086/346020.

Spiegel, E.A., and Zahn, J.-P.: 1992, *Astronomy and Astrophysics*, **265**, 106–114.

Matilsky, L.I., Brummell, N.H., Hindman, B.W., and Toomre, J.: 2024, *The Astrophysical Journal* **962**, 189. doi:10.3847/1538-4357/ad18b2.

Miesch, M.S., Brun, A.S., and Toomre, J.: 2006, *The Astrophysical Journal* **641**, 618. doi:10.1086/499621.

Thompson, M.J., Christensen-Dalsgaard, J., Miesch, M.S., and Toomre, J.: 2003, *Annual Review of Astronomy and Astrophysics* **41**, 599. doi:10.1146/annurev.astro.41.011802.094848.

Rudiger, G. and Kitchatinov, L.L.: 1997, *Astronomische Nachrichten* **318**, 273. doi:10.1002/asna.2113180504.

Leprovost, N. and Kim, E.-J.: 2006, *Astronomy and Astrophysics* **456**, 617. doi:10.1051/0004-6361:20065265.

Tomczyk, S., Streander, K., Card, G., Elmore, D., Hull, H., and Cacciani, A.: 1995, *Solar Physics* **159**, 1. doi:10.1007/BF00733027.

Harvey, J. W., Hill, F., Hubbard, R. P., Kennedy, J. R., Leibacher, J. W., Pintar, J. A., Gilman, P. A., Noyes, R. W., Title, A. M., Toomre, J., Ulrich, R. K., Bhatnagar, A., Kennewell, J. A., Marquette, W., Patron, J., Saa, O., and Yasukawa, E.: 1996, *Science* **272**, 1284. doi:10.1126/science.272.5266.1284.

Scherrer, P. H., Bogart, R. S., Bush, R. I., Hoeksema, J. T., Kosovichev, A. G., Schou, J., Rosenberg, W., Springer, L., Tarbell, T. D., Title, A., Wolfson, C. J., and Zayer, I.: 1995, *Solar Physics* **162**, 129. doi:10.1007/BF00733429.

Schou, J., Scherrer, P. H., Bush, R. I., Wachter, R., Couvidat, S., Rabello-Soares, M. C., Bogart, R. S., Hoeksema, J. T., Liu, Y., Duvall, T. L., Akin, D. J., Allard, B. A., Miles, J. W., Rairden, R., Shine, R. A., Tarbell, T. D., Title, A. M., Wolfson, C. J., Elmore, D. F., Norton, A. A., and Tomczyk, S.: 2012, *Solar Physics* **275**, 229. doi:10.1007/s11207-011-9842-2.

Libbrecht, K.G.: 1989, *The Astrophysical Journal* **336**, 1092. doi:10.1086/167079.

Basu, S. & Antia, H. M. 2003, ApJ, 585, 1, 553. doi:10.1086/346020